Electrochimica Acta 504 (2024) 144893

Contents lists available at ScienceDirect

Electrochimica Acta

journal homepage: www.journals.elsevier.com/electrochimica-acta

Molybdate and vanadate ions as corrosion inhibitors for clad aluminium alloy 2024-T3

Ingrid Milošev [a,*], Tjaša Pavlovčič [b], Matija Tomšič [b]

[a] Jožef Stefan Institute, Department of Physical and Organic Chemistry, Jamova cesta 39, SI-1000 Ljubljana, Slovenia
[b] University of Ljubljana, Faculty of Chemistry and Chemical Engineering, Večna pot 113, SI-1000 Ljubljana, Slovenia

ARTICLE INFO

Keywords:
Aluminium alloy
Clad AA2024-T3
Molybdate
Vanadate
Corrosion inhibitors
Aqueous chemistry
XPS
SEM

ABSTRACT

Molybdate and vanadate ions were used as corrosion inhibitors for the clad aluminium alloy 2024-T3 in chloride solution to investigate the differences in their inhibitory effect. Electrochemical measurements in 0.1 M NaCl investigated the influence of inhibitor concentration from 0.5 mM to 250 mM, solution pH from 5 to 9 and immersion time at open circuit potential of up to 12 h. Both compounds act predominantly as anodic inhibitors; however, the effect of molybdate increases significantly at concentrations above 50 mM and leads to a broad passive range. Surface analysis of the samples exposed to inhibitor performed by X-ray photoelectron spectroscopy showed that the inhibitor layers consist of oxides of multiple valences. Scanning electron microscopy with chemical analysis was also used to characterise the inhibitor layers. Equilibrium diagrams of the aqueous species in the selected concentration range were generated to better understand the inhibition mechanism and to correlate the electrochemical data and data on surface properties.

1. Introduction

Replacing toxic and environmentally hazardous compounds with those less toxic and harmful is the common red thread in today's research in a broad spectrum of scientific fields, including corrosion protection. One of the notable examples of hazardous compounds with excellent corrosion protection ability is hexavalent chromate anions; the activities directed towards replacing chromates were initiated almost 20 years ago [1–4] and are still ongoing [5]. The compounds to replace chromates should not be hazardous, or at least much less, and, at the same time, equally fulfil the given performance task, i.e., to act as effective corrosion inhibitors. In this study, we chose two viable alternatives, i.e. molybdate and vanadate anions.

Let us first consider their production, environmental exposure, toxicity and carcinogenicity. Molybdenum trioxide (MoO_3) is the most important chemical product of molybdenite (MoS_2). MoO_3 is used mainly in steel and alloy production [6]. Environmental exposures to MoO_3 are inconsiderable, whereas occupational exposures are mainly related to mining and metallurgy processing of steel [7]. Vanadium pentoxide (V_2O_5), the major commercial vanadium product, is mainly used as a catalyst in the production of iron and aluminium alloys. It is also used as an oxidation catalyst in the chemical industry. Exposure to V_2O_5 in the workplace occurs during the refining and processing V-rich mineral ores, burning fossil fuels, especially petroleum, handling vanadium catalysts in the chemical manufacturing industry, and cleaning oil-fired boilers and furnaces. The major non-cancer health effect of inhalation exposure to V_2O_5 involves acute respiratory irritation, characterized as `boilermakers bronchitis' [8].

According to the International Agency for Research on Cancer (IARC), chromate compounds are classified as cancerogenic to humans (designated as Group 1) [9]. The potential human toxicity of molybdate and vanadate is lower than that of chromate: both MoO_3 and V_2O_5 belong to the same category in terms of carcinogenicity, i.e. possibly carcinogenic to humans (designated as Group 2B)[1] as shown in Table 1 [7,8]. No human carcinogenic data are available. V_2O_5 is mutagenic in vitro and possibly in vivo in mice [8]. According to the Occupational Safety and Health Administration (OSHA) Hazard Communication Standard (HCS) [9], sodium molybdate (Na_2MoO_4) and sodium vanadate ($NaVO_3$) differ in their

* Corresponding author.
E-mail address: ingrid.milosev@ijs.si (I. Milošev).

[1] There is inadequate evidence in humans for their carcinogenicity but there is sufficient evidence in experimental animals for their carcinogenicity.

https://doi.org/10.1016/j.electacta.2024.144893
Received 1 June 2024; Received in revised form 12 August 2024; Accepted 12 August 2024
Available online 13 August 2024

Table 1
Data on toxicity and carcinogenicity for sodium chromate, vanadate and molybdate [10–12].

Compound	LD_{50} oral [mg/kg]	LC_{50} inhalation [mg/m^3]	Carcinogenicity
Sodium chromate	136 (rat)	104 (rat)	Group 2B
Sodium vanadate	330 (rat)	Not listed	Group 2B
Sodium molybdate	4000 (rat)	>2080	Group 1

classification: Na_2MoO_4 is not a hazardous chemical [10],[2] whereas $NaVO_3$ is considered hazardous [11],[3] For comparison, sodium chromate (Na_2CrO_4) [12] is also classified as hazardous, but is classified[4] as much severely dangerous than $NaVO_3$ [11].

The differences in toxicity can be compared by the lethal dose[5] (LD_{50}) or the exposure concentration LC_{50}, which is lethal to 50 % of exposed animals (rats; Table 1). LD_{50} for sodium vanadate is only 2.4 times larger than sodium chromate, while 30 times larger for sodium molybdate [10–12].

Throughout the last decades, molybdate and vanadate have been investigated as corrosion inhibitors and potential chromate replacements. Recently, Milošev published a comprehensive review on corrosion inhibition of aluminium alloys by molybdate ions in aqueous solutions and cooling systems [13]. The actions of molybdate as an individual inhibitor and incorporated as fillers, pigments and nanocontainers into various coatings were presented [13]. Molybdate has been known as a corrosion inhibitor for over 80 years since it was patented in 1939 by Bayes [14]. Vukasovich and Farr reviewed the development of various formulations [15]. The inhibition effect of molybdate was extensively studied on iron and steel [16]. Molybdate is classified as an anodic inhibitor, but it requires the presence of oxygen or an oxidizing agent in the solution [17,18]. The inhibitive action of molybdate with the surface of aluminium alloys has been studied in numerous papers [18–26]. Milošev recently summarized different mechanisms of molybdate inhibitive action of Al metal and Al alloys [13].

Another interesting issue concerning both molybdate and vanadate is the possibility of a synergistic combination. The synergistic effect of molybdate with rare earth cations (lanthanum and cerium) was identified in corrosion inhibition, which even outperformed the one exhibited by the chromate anions [27–30]. The synergism of molybdate with other species was also identified: with nitrite [14,31] on various metals, silicate on AA2024-T3 [32], lanthanum as zeolite microparticles in a sol–gel coating on AA2024-T3 [33], cerium as nanowires [34] or nanocontainers in an epoxy coating [35] on AA2024-T3, added in an anodized layer formed in tartaric/sulphuric acid grown in AA2024-T3 [36], intercalated with layered double hydroxides (LDHs) on AA2024-T3 [37] and combined with phosphate, citrate and benzimidazole/benzothiazole on AA7075-T76 [38]. In addition, molybdate is used as a basis for conversion coatings on various aluminium alloys [39–42], zinc [43,44] and magnesium alloys [45].

In contrast to molybdate, vanadate has been investigated as a viable corrosion inhibitor less intensively. Vanadates as corrosion inhibitors were summarized by Hinton [2,3] and addressed by Kendig and Buchheit as a possible substitute for chromate compounds together with molybdate [1]. Vanadate in the form of conversion coating increased the pitting potential of AA2024-T3 in near-neutral solutions and increased the oxygen reduction reaction (ORR) rate. The coatings consisted of vanadium oxides in several oxidation states and could self-heal after scratching [46]. Similar to molybdate, vanadate inhibited cathodic kinetics only in aerated solutions, mainly by suppressing Al_2CuMg intermetallic particle (IMP) dissolution [47]. An order of magnitude reduction in corrosion current density was observed at pH 8 and 10, and a positive shift of pitting potential for 200 mV. Tetrahedrally coordinated forms of vanadate (ortho-, pyro and metavanadates) acted inhibitory, but orange octahedrally (decavanadates) forms did not provide inhibition [47]. The degree of inhibition was dependent on the type of Al alloy: for AA7075 and AA6061, which contain less Cu-based IMPs, the inhibition by vanadate was not strictly cathodically dominated but, with time, became mixed or even anodic [48]. The inhibition performance of vanadate on AA2024-T3 was studied from 10 to 80 °C [49]. The film formed at higher temperatures was thicker on IMPs and the matrix. Reducing V(V) on the metal surface during exposure was proposed to enhance subsequent polymerization promoted at higher temperatures [49]. Ianuzzi and Frankel conducted extensive studies of corrosion inhibition of AA2024-T3 by vanadate [50–52]. The effective action of vanadate was also investigated against atmospheric pitting corrosion of AA7075-T6 under evaporating droplets [53]. Kharitonov et al. reported three studies on corrosion inhibition of AA6063-T5 by vanadate [54,55,56]. Adsorbed vanadate provided mixed corrosion inhibition effects, mitigating both ORR on cathodic IMPs and anodic metal dissolution, mainly on Mg_2Si and interphase boundary regions [55].

The synergy of metavanadate with phosphate was reported to surpass that of chromate; synergy was also observed with molybdate and silicate [27–30]. In addition to being used as an aqueous corrosion inhibitor, vanadate was applied in versatile combinations and applications on aluminium alloys: (i) as LDHs nanocontainers loaded with vanadate, phosphate and 2-mercaptobenzothiazolate [57] and nanostructured double Mg/Al and Zn/Al hydroxides with divanadate anions on AA2024 [58], (ii) as nanocontainers loaded into sol–gel coatings [59] and as binary layers comprising LDH conversion layer loaded with vanadate [60] and other inhibitors [37,61,62] and covered with a sol–gel layer, (iii) as epoxy-based composite coating containing Al flakes covered with vanadate-doped polypyrrole on AA2024-T3 [63], (iv) in the form of conversion coating on AA2024-T3 [46,64,65], and (v) as post-treatment for anodized Al and AA2024-T3 [66]. In addition to aluminium alloys, vanadate as an inhibitor or conversion coating was studied on Zn [43,67], Mg alloys [68,69], and hot-dip galvanized steel [70].

An advantage of vanadate is the possibility of self-healing, which has been demonstrated as conversion coating tested in a scratch test [46], or LDH conversion inner layers [57–59], thus achieving similar action as traditional chromate coatings [1].

Literature review shows that the possibilities of using molybdate and vanadate as individual inhibitors, conversion coatings, or in different synergistic combinations as inhibitors, nanocontainers or bilayers are broad and still open to numerous research options. On aluminium alloys, the majority of studies have dealt with AA2024-T3, with Cu-rich IMPs being the main promotor of localized corrosion. In the present study, we used clad AA2024-T3 since no previous study has been performed on this substrate concerning molybdate and vanadate. Generally, the cladding layers (Alclad) are selected as anodic to the core metal, thereby providing corrosion protection. Alclad sheet is widely used in applications requiring a combination of good mechanical properties and good corrosion resistance, as in the manufacture of commercial aircrafts.

[2] This chemical is not considered hazardous by the 2012 OSHA Hazard Communication Standard (29 CFR 1910.1200) [10].

[3] This chemical is considered hazardous by the 2012 OSHA Hazard Communication Standard: Acute oral toxicity: 4; Skin and eye irritation: 2; Specific target organ toxicity: 3, where the number represents the category, 1 is the most and 4 the least hazardous [11].

[4] This chemical is considered hazardous by the 2012 OSHA Hazard Communication Standard (29 CFR 1910.1200): Acute oral toxicity: 3; Acute dermal toxicity: 4; Acute Inhalation toxicity: 2; Skin Irritation: 1B; Eye irritation: 1; Respiratory senzitation: 1; Skin senzitation: 1; Carcinogenicity: 1A; Germ cell mutagenicity: 1B; Reproductive toxicity: 1B; Specific target organ toxicity (single exposure): 3; Specific target organ toxicity (repeated exposure), where the number represents the category, 1 is the most and 4 the least hazardous [12].

[5] Lethal dose (LD_{50}) is the amount of a chemical that is lethal to one-half (50 %) of the experimental animals exposed to it.

2. Experimental

2.1. Equilibrium and fraction diagrams

Equilibrium diagrams log(c) vs. pH and fraction diagrams of molybdenum and vanadium species in solution were constructed using Hydra/Medusa software programme, which already contains data on equilibrium constants at 25 °C [71]. Species present in the solution were selected at determined concentration.

2.2. Material and chemicals

The chemical composition of clad aluminium alloy AA2024-T3 was provided by supplier Kaiser Aluminium, Trentwood, USA, as 4.35 wt.% Cu, 1.33 wt.% Mg, 0.53 wt.% Mn, 0.25 wt.% Fe, 0.19 wt.% Cr, 0.09 wt.% Si, 0.08 wt.% other elements, and 93.18 wt.% Al. The cladding process included clad liner plates, cast and rolled, assembled and heated as a unit with AA2024-T3. Flat sheets, 0.5 mm thick, were cut into 1.5 cm × 1.5 cm samples. The clad layer is made of AA1230 alloy consisting of ≥99.3 wt.% Al, ≤0.70 wt.% Si + Fe, ≤0.10 wt.% Zn, ≤0.10 wt.% Cu, ≤0.05 wt.% Ti, ≤0.05 wt.% V, ≤0.05 wt.% Mg, ≤0.05 wt.% Mn and ≤0.03 wt.% other. According to the supplier, the minimum average clad thickness is 4 %, ca. 20 μm.

Before each measurement, the samples were first water-ground on SiC papers sequentially to 4000 grit; samples were then rinsed with deionized water, cleaned in ethanol in an ultrasonic bath for 2 min and dried with a nitrogen stream. Samples were then subjected to diamond grinding on an MD-Piano 1200 disc using a DP-Lubricant Blue non-water-based lubricant liquid, followed by the same cleaning step as after the first grinding step. All grinding items were supplied by Struers (Ballerup, Denmark).

The corrosive medium was 0.1 M NaCl solution (pH = 5.9) prepared using sodium chloride, NaCl (≥99.5 %, Fischer Scientific) and Milli-Q Direct water with 18.2 MΩ·cm resistivity at 25 °C (Millipore, Billerica, MA). Sodium molybdate dihydrate $Na_2MoO_4{\cdot}2H_2O$ (abbreviated Na_2MoO_4, ≥99.5 % Honeywell Fluka) and sodium vanadate, $NaVO_3$ (≥98 %, Aldrich) were tested as potential corrosion inhibitors. Other chemicals used were absolute ethanol, EtOH (Carlo Erba), sodium hydroxide, NaOH (≥99 %, Merck), and hydrochloric acid, HCl (37 %, Honeywell Fluka) for pH regulation.

Na_2MoO_4 and $NaVO_3$ were added to 0.1 M NaCl at concentrations 0.5, 1, 5, 10, 50, 100, 150 and 250 mM. Depending on the concentration, the addition of Na_2MoO_4 changed the pH of 0.1 M NaCl from 5.9 to 9.2, and the addition of $NaVO_3$ from 5.9 to 7.2. An 827 pH Lab Metrohm pH meter was used for measurements.

2.3. Electrochemical measurements

Electrochemical measurements were conducted with an Autolab PGSTAT 204 potentiostat/galvanostat controlled by Nova 2.0 software. Measurements were performed in aerated 0.1 M NaCl at room temperature in a three-electrode corrosion cell (PAR Flat cell K0235, volume 250 mL). Working and counter electrodes were placed in a hole on each end plate of the cell. Samples, pressed against the central hole of the wall using an encapsulated silicone o-ring and with an exposed nominal area of 1 cm^2 to corrosive medium, served as working electrodes. A platinum mesh was used as a counter electrode. The reference electrode bridge tube is a vertical tube with an Ag/AgCl/saturated KCl electrode (E = +0.197 V vs. standard hydrogen electrode, SHE).

Before measurement, all substrates were allowed to stabilize for 2 h in electrolyte solution under open circuit conditions. In some experiments, a stabilization time of 12 h was used. The stable, quasi-steady state potential, open circuit potential, E_{oc}, is taken as being established when the potential does not vary more than ±3 mV/min. The linear polarisation measurements were performed in a potential range of ±10 mV vs. E_{oc}, using a 0.1 mV/s potential scan rate. The polarisation resistance (R_p) values were deduced from the slope of fitted current density vs. potential curves. Potentiodynamic measurements followed, starting at 250 mV negative to E_{oc} and increasing in the anodic direction. The potential scan rate was 1 mV/s. The corrosion current density (j_{corr}), corrosion potential (E_{corr}) and anodic and cathodic Tafel slopes (β_a and β_c) were determined from anodic and cathodic Tafel curves using Nova software 2.1. The breakdown potential (E_{br}) was determined as the potential of an abrupt increase in anodic current density. The potential span between E_{corr} and E_{br} is defined as $\Delta E = |E_{corr} - E_{br}|$ and is taken as a measure of susceptibility to pitting corrosion, i.e., the larger the extent, the smaller the susceptibility. Measurements were repeated at least three times to ensure reproducibility. Representative potentiodynamic curves (determined based on at least two close repetitions) are presented in plots; electrochemical parameters deduced from representative measurements are given in tables.

2.4. Surface analysis

A scanning electron microscope (SEM) JSM 7600-F (JEOL) and an energy dispersive X-ray spectroscopy (EDS) INCA 350 (Oxford Instruments) were used to analyse the morphology and composition of the samples' surfaces. SEM analysis was carried out using secondary electrons (SE mode) and backscattered electrons (Compo mode) at an acceleration voltage of 15 kV. Before analysis, samples were not coated.

Selected analyses were conducted using field-emission SEM/EDS. FEI Helios Nanolab 650 microscope, equipped with EDS (Oxford Instruments Aztec system with X-max SDD detector), was employed to deposit two Pt protection layers—electron-beam-assisted and ion beam (Ga^+)-assisted ones with thicknesses of 0.2 and 1 μm, respectively. A trench was then opened by milling under rough conditions with Ga^+ ions of 2.5 nA at 30 kV, followed by rough polishing (0.77 nA, 30 kV) and fine polishing (0.4 nA, 30 kV). Within the trench, the cross-section across the S-phase and the substrate was analysed by SEM-EDS in SE mode at an accelerating voltage of 5 kV.

X-ray photoelectron spectroscopy (XPS) analysis was performed using a PHI 5600 (Physical Electronics, US) spectrometer with an X-ray source Al Kα (1486.6 keV). The diameter of the analyzed spot at the sample was 0.8 μm × 0.8 μm. Energy and time resolution were 0.2 eV/scan and 25 s/scan, respectively, and the pass energy was 23.5 eV. The position of the peaks was adjusted to that of the C 1s peak at a binding energy (E_b) of 284.8 eV, and the Multipak software, version 8.1 (Physical Electronic Inc), was used. Carbon as an adventitious element was not considered when calculating the surface elemental composition.

The fitting procedure was carried out using an XFIT programme [72]. It allowed signals to be evaluated by determining peak positions, height, width and the ratio representing the Gaussian/Lorentzian nature of the peak. The border positions were fixed by parameters of standard peaks.

3. Results and discussion

3.1. The aqueous chemistry of molybdenum and vanadium

In a chemical sense, molybdenum and vanadium are very complex. Although the passivity ranges of Mo and V are not very broad, and as such, they would not be very interesting for corrosion protection [1,73]. The chemistry of their aqueous anions is versatile and offers a broad range of possible chemical and electrochemical reactions. Molybdate (MoO_4^{2-}) and vanadate (VO_4^{3-}) anions belong to transition elements under high oxidation states, i.e. V(V) and Mo(VI), and in their maximum oxidation state, in an alkaline medium, exist as tetraoxo monomers $[MO_4]^{(8-z)-}$ [74]. These oxygen cluster anions of early transition metals, polyoxometalates (POMs), can be divided into isopolyoxymetalates and heteropolyoxometalates, depending on whether they contain only transition anion (isopoly-) or additional hetero anion (heteropoly-, e.g. phosphorus or silicon). Depending on the pH, condensation of vanadate

leads to pyro-, meta- and decavanadate formation, whereas molybdate condenses to para- and octamolybdates [74,75].

Fig. 1 presents fraction diagrams of species vs. pH constructed using the Medusa programme for Na_2MoO_4 concentrations of 1, 10, 50 and 150 mM. Diagrams for all concentrations investigated given as equilibrium diagrams log(*c*) vs. pH are shown in Fig. S1 in the Supplement.

At pH > 6, molybdate tetraoxo $[MoO_4]^{2-}$ monomer ions are a prevailing species [13]. At more acidic pH, at pH < 5, protonated $[HMoO_4]^-$ and H_2MoO_4 are formed. Upon the addition of concentrated nitric acid, yellow hydrated molybdenum(VI) oxide precipitates as $MoO_3{\cdot}xH_2O$ (also denoted as molybdic acid $H_2MoO_4{\cdot}H_2O$).

The acidic region is characterised by the formation of polynuclear species (see Figs. 1 and S1), especially at higher Mo concentrations ($>10^{-4}$ M). The predominant species is heptamolybdate (paramolybdate), formed according to [74]:

$$7\ [MoO_4]^{2-} + 8H^+ \longrightarrow [Mo_7O_{24}]^{6-} + 4H_2O \quad (1)$$

Between pH 5 and pH 3, these species coexist with their protonated forms $[HMo_7O_{24}]^{5-}$ (pK = 4.4), $[H_2Mo_7O_{24}]^{4-}$ (pK = 3.5), $[H_3Mo_7O_{24}]^{3-}$ (pK = 2.5) [13,74]. The formation of polynuclear species involves a change in Mo coordination from tetrahedral to octahedral.

It should be noted that thermodynamic data for Mo species vary depending on the databases used [76], especially concerning considerable variation in the dominant polynuclear species present at high Mo concentrations and low pH and the range of stability of intermediate $HMoO_4^-$ species.[6]

In the investigated concentration range between 0.5 mM and 250 mM, the pH of the NaCl solution with added molybdate is between 7 and 9.2, where $[MoO_4]^{2-}$ is predominantly stable (see Fig. 1). Polynuclear Mo species are formed at pH lower than 7 and do not contribute significantly at the pH of tested solutions. The increase in molybdate concentration is related to the increase in pH mainly due to the increased contribution of MoO_4^{2-} and $HMoO_4^-$. The former strongly increased at concentrations higher than 50 mM. Under those conditions, the contribution of $HMoO_4^-$ also increased.

Fig. 2 presents fraction diagrams of species vs. pH constructed using the Medusa programme for $NaVO_3$ concentrations of 1, 10, 50 and 150 mM. Diagrams for all concentrations investigated given as equilibrium diagrams log(*c*) vs. pH are shown in Fig. S2 in the Supplement. Vanadate exists in several aqueous species [47,50,73,74,77]. At high pH values (pH < 13), orthovanadate (VO_4^{3-}) and VO_3OH^{2-} species dominate in all solutions. At pH between 9 and 12, orthovanadate can combine to form pyrovanadates $[V_2O_7^{4-}$, $HV_2O_7^{3-}$, and $VO_3(OH)^{2-}]$ [74]:

$$2\ [VO_4]^{3-} + 2H^+ \longrightarrow [V_2O_7]^{4-} + H_2O \quad (2)$$

$$2\ [VO_3(OH)]^{2-} \longrightarrow [V_2O_7]^{4-} + H_2O \quad (3)$$

Between pH 6 and 9, metavanadates $[V_3O_9^{3-}$, $V_4O_{12}^{4-}$, $V_5O_{15}^{5-}$, $VO(OH)_3$ and $VO_2(OH)_2^-]$ can form [47,74]:

$$4\ [VO_4]^{3-} + 8H^+ \longrightarrow [V_4O_{12}]^{4-} + 4H_2O \quad (4)$$

$$4\ [VO_2(OH)_2]^- \longrightarrow [V_4O_{12}]^{4-} + 4H_2O \quad (5)$$

Both ortho- and pyrovanadates are colourless. As the concentration of sodium vanadate increases in strongly basic solutions, the concentration of $V_2O_7^{4-}$ increases. By acidification from pH 3 to 6, the vanadate solution becomes orange or red due to the formation of octahedral decavanadates [74].

$$10\ [VO_4]^{3-} + 25H^+ \longrightarrow [HV_{10}O_{28}]^{5-} + 12H_2O \quad (6)$$

$$5\ [VO_2(OH)_2]^- + 5\ [VO(OH)_3] \longrightarrow [HV_{10}O_{28}]^{5-} + 12H_2O \quad (7)$$

[6] The OECD Nuclear Energy Agency (NEA) Thermochemical Database Project (TDB) is currently running a project of reviewing thermodynamic data on Mo and expected to be published next year.

In strongly acidic solutions (pH < 3), pervanadyl VO_2^+ and $VO(OH)_3$ dominate [74].

In the investigated concentration range between 0.5 mM and 250 mM, the pH of the NaCl solution with added vanadate is between 6 and 7 and does not change significantly with concentration (see Fig. 2). At these pH values, the metavanadates $VO_2(OH)_2^-$, $V_3O_9^{3-}$ and $V_4O_{12}^{4-}$ dominate in the solution. At higher concentrations of sodium vanadate in the solution, an increase in $V_3O_9^{3-}$ ions was observed. At concentrations higher than 50 mM, condensation of vanadate ions occurs in the solution, forming metavanadates $V_4O_{12}^{4-}$ and also decavanadates $V_{10}O_{28}^{6-}$. The solution coloured pale orange and became dark orange with time, the colour characteristic of decavanadates.

3.2. The effect of molybdate and vanadate anions added to NaCl on the electrochemical behaviour

The potentiodynamic polarization curve for clad AA2024-T3 in 0.1 M NaCl is given in Fig. 3. After 2 h, E_{oc} was stabilized at −0.71 V. Deduced electrochemical parameters are presented in Table S1. Polarization resistance (R_p) with 54 kΩ cm^2 is higher than that of unclad AA2024-T3 with R_p of 16 kΩ cm^2 [78]. The polarization curve also confirmed improved corrosion resistance of the clad alloy due to the passive range with width (ΔE) of 160 mV limited by the breakdown potential at −0.58 V. In comparison, bare AA2024-T3 exhibits ΔE of only 30 mV and six times larger corrosion current density (j_{corr}) [78]: 1.9 μA cm^{-2} compared to 0.31 μA cm^{-2} (see Table S1). The cathodic polarization curve is related to the reduction of dissolved oxygen, and the anodic part is to the oxidation of aluminium in the clad, resulting in the formation of aluminium oxide. It assures protection in the passive range before the abrupt increase of the current density at the breakdown potential (E_{br}) due to the localized corrosion induced by chloride ions [79].

Potentiodynamic polarization curves recorded in 0.1 M NaCl with added Na_2MoO_4 in the range from 5 mM to 250 mM are shown in Fig. 3. Related electrochemical results are presented in Fig. 4 and Table S1. Electrochemical parameters of molybdate addition show two distinct regions of linearity. The straight lines of j_{corr} as a function of the logarithm of molybdate concentration, log $c_{molybdate}$, show two distinct regions (Fig. 4a). In the concentration range from 0.5 mM to 50 mM (log −3.3 and −1.3), j_{corr} decreased with increasing concentration from 0.19 to 0.13 μA cm^{-2}. However, at larger concentrations, j_{corr} increased rather steeply and reached 1.6 μA cm^{-2} at 250 mM (log −0.6). Interestigly, for $c_{molybdate} \leq 50$ mM, E_{corr} shifted slightly more positively, while at higher concentrations, the trend reversed, attaining a steep negative slope (Fig. 4b). For E_{br}, the trend was just the opposite; a steep positive slope accompanied concentrations above 50 mM (Fig. 4c). Consequently, due to the negative shift in E_{corr} and positive shift in E_{br}, ΔE extended considerably for $c_{molybdate} > 50$ mM (Fig. 4d), reaching 920 mV at 250 mM Na_2MoO_4 (Fig. 3). However, the broadening of ΔE was accompanied by increased j_{corr}.

Two distinct regions of linear dependency of electrochemical parameters on molybdate addition can be related to the change in pH (Fig. 4e) and the change in aqueous chemistry (Fig. 2), as discussed in the text above. For $c_{molybdate} \leq 50$ mM, NaCl solution's pH with added Na_2MoO_4 is between 6.9 and 7.6. However, for $c_{molybdate} > 50$ mM, pH steeply increased to 9.2. When relating these findings with chemical equilibrium diagrams in Fig. 2, it is evident that the increase in pH is related to increased content of MoO_4^{2-} and $HMoO_4^-$ at $c_{molybdate} > 50$ mM.

Potentiodynamic polarization curves recorded in 0.1 M NaCl with added $NaVO_3$ in the range from 5 mM to 250 mM and related electrochemical results are presented in Fig. 5. Related electrochemical results are presented in Table S2 and Fig. 4, together with those for molybdate. In contrast to molybdate, the dependences of electrochemical parameters follow the same linearity trend in the whole concentration range investigated. The dependence of j_{corr} on the logarithm of vanadate concentration, log $c_{vanadate}$, is linear (Fig. 4a), giving a declining straight

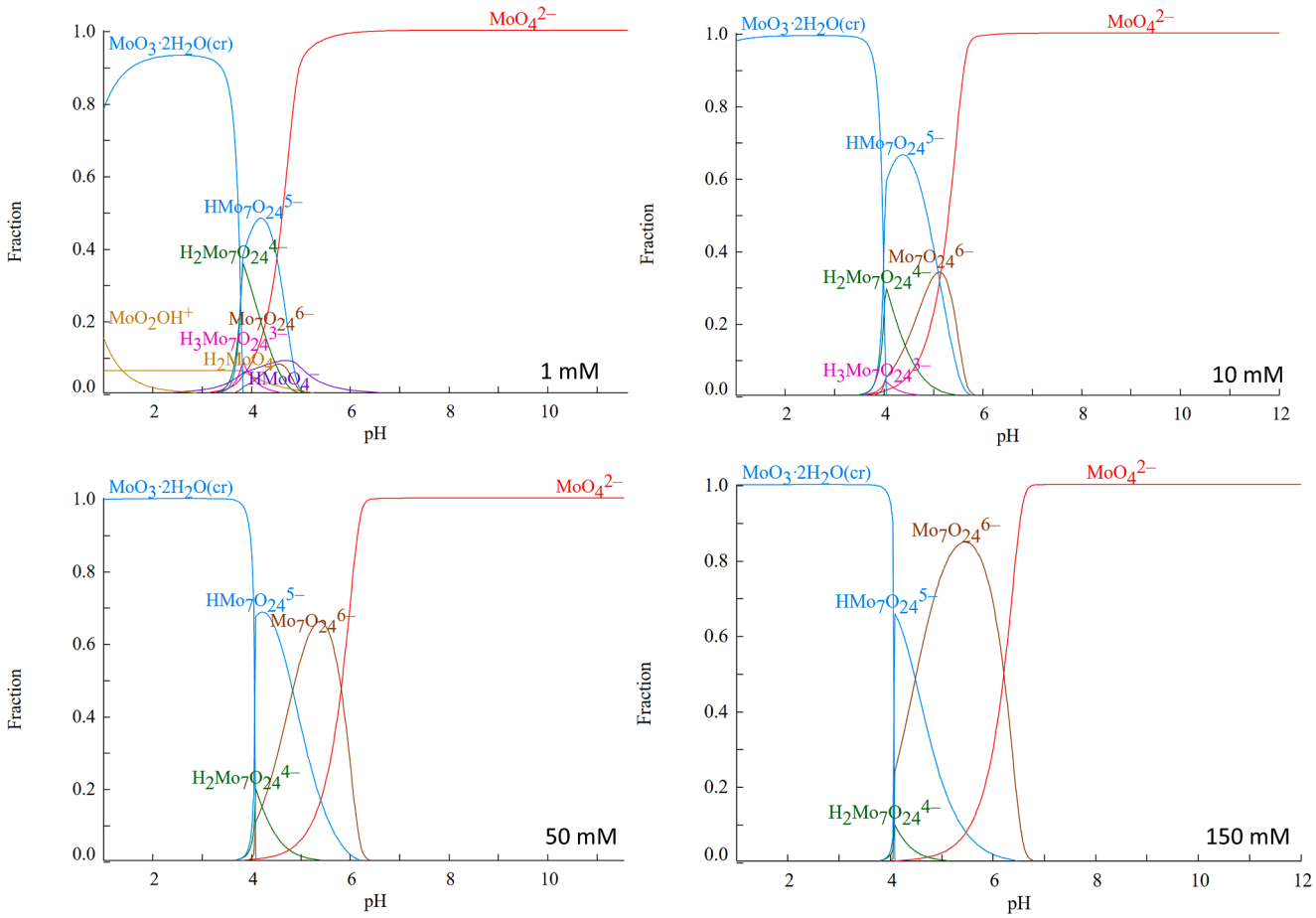

Fig. 1. Fraction vs. pH for species at selected concentrations of Na_2MoO_4 (1, 10, 50 and 150 mM) in 0.1 M NaCl solution. The diagrams were generated using Medusa software. Equilibrium log(*c*) vs. pH diagrams calculated for all concentrations investigated are given in Fig. S1.

line of $j_{corr} = -0.006 \log c_{vanadate} + 0.11$, i.e. with a similar slope as for the addition of molybdate in the same concentration range. The dependence of E_{corr} on the log $c_{vanadate}$ is also linear (Fig. 4b), giving a relationship $E_{corr} = 0.075 \log c_{vanadate} - 0.59$ with E_{corr} ranging between −0.74 V and −0.66 V. A similar trend is observed for E_{br}: it shifted in the positive direction from −0.61 V to −0.53 V (Fig. 4c). Since the negative trend of E_{corr} with increasing $c_{vanadate}$ is steeper than a concomitant positive trend of E_{br}, ΔE does not increase substantially with increasing concentration but remained within −30 mV and + 80 mV relative to the value in noninhibited NaCl solution (i.e. $\Delta E = -0.041 \log c_{vanadate} + 0.092$, Fig. 4d). However, both cathodic and anodic current densities are reduced reflecting that VO_3^- acts as a mixed inhibitor but with a more substantial effect on the anodic side at $c_{vanadate} \geq 50$ mM.

Depending on the concentration, the addition of $NaVO_3$ in 0.1 M NaCl increased the pH from 5.9 to 6.3 (at 5 mM) and 7.2 (at 250 mM) (Fig. 4e). Although the pH does not change significantly, the chemical equilibrium diagrams (Fig. 2) show that the increase in concentration is related to increasing concentration of metavanadate $V_4O_{12}^{4-}$ and also decavanadate $V_{10}O_{28}^{6-}$.

Fig. 6 compares polarization curves recorded in 0.1 M NaCl with and without added $NaVO_3$ and Na_2MoO_4 for each concentration separately. Notably, up to 50 mM vanadate and molybdate anions have similar effects on the electrochemical response of clad AA2024-T3. Additions above 50 mM, however, resulted in a substantial extension of ΔE for molybdate but at the expense of somewhat higher current densities. For vanadate, ΔE followed the same trend as at smaller concentrations, but j_{corr} further decreased. Therefore, it seems that for $c > 50$ mM, the inhibition by vanadate ions has a more significant effect on the corrosion current density and by molybdate ions on the extension of the passive range.

At 150 mM additions of vanadate and molybdate to 0.1 M NaCl solutions the effect of immersion time at E_{oc} and the effect of solution pH were also investigated. Prolonged immersion at E_{oc} from 2 to 12 h slightly improved the electrochemical parameters for vanadate, with j_{corr} reducing from 0.05 to 0.03 μA cm^{-2} and E_{corr} shifted negatively for 20 mV (see Fig. 7 and Table S3). For molybdate, however, the effect was more substantial: not only that ΔE increased from 740 mV to 950 mV, but j_{corr} reduced. Therefore, the action of molybdate improves with immersion time, indicating that the inhibition process is dynamic and involves sequential reactions.

The pH value of the solution is an essential parameter for the overall inhibition effect (see Fig. 8 and Table S4). With addition of 50 mM of $NaVO_3$ and Na_2MoO_4 to 0.1 M NaCl with the pH value of 5.9, the pH value of the solution changed to 7.1 and 8.9, respectively. In addition to investigating the solutions with naturally attained pH after vanadate and molybdate addition, the measurements were also carried out in two solutions with adjusted pH values: for vanadate, pH was adjusted to 5 and 9, and for molybdate to 5 and 7. In a more acidic solution (pH 5), the polarization curve in solution with 0.1 M NaCl and 150 mM $NaVO_3$ shifted to higher current densities with no notable inhibition effect. In a more alkaline solution (pH 9) than natural pH (pH 7.1), E_{corr} shifted to more negative values, leading to the broadening of ΔE from 120 mV to 240 mV. Therefore, a slightly higher pH than the natural one is still suitable for the inhibiting action of vanadate on clad AA2024-T3.

For the molybdate solution, the pH effect was more pronounced (see Fig. 8 and Table S4). A decrease in pH from 8.9 to 7 resulted in a loss of inhibition effect, while at pH 5, it acted as an activator, similar to vanadate. Therefore, the best inhibitive effect of both vanadate and molybdate was achieved at the natural pH attained after adding these ions.

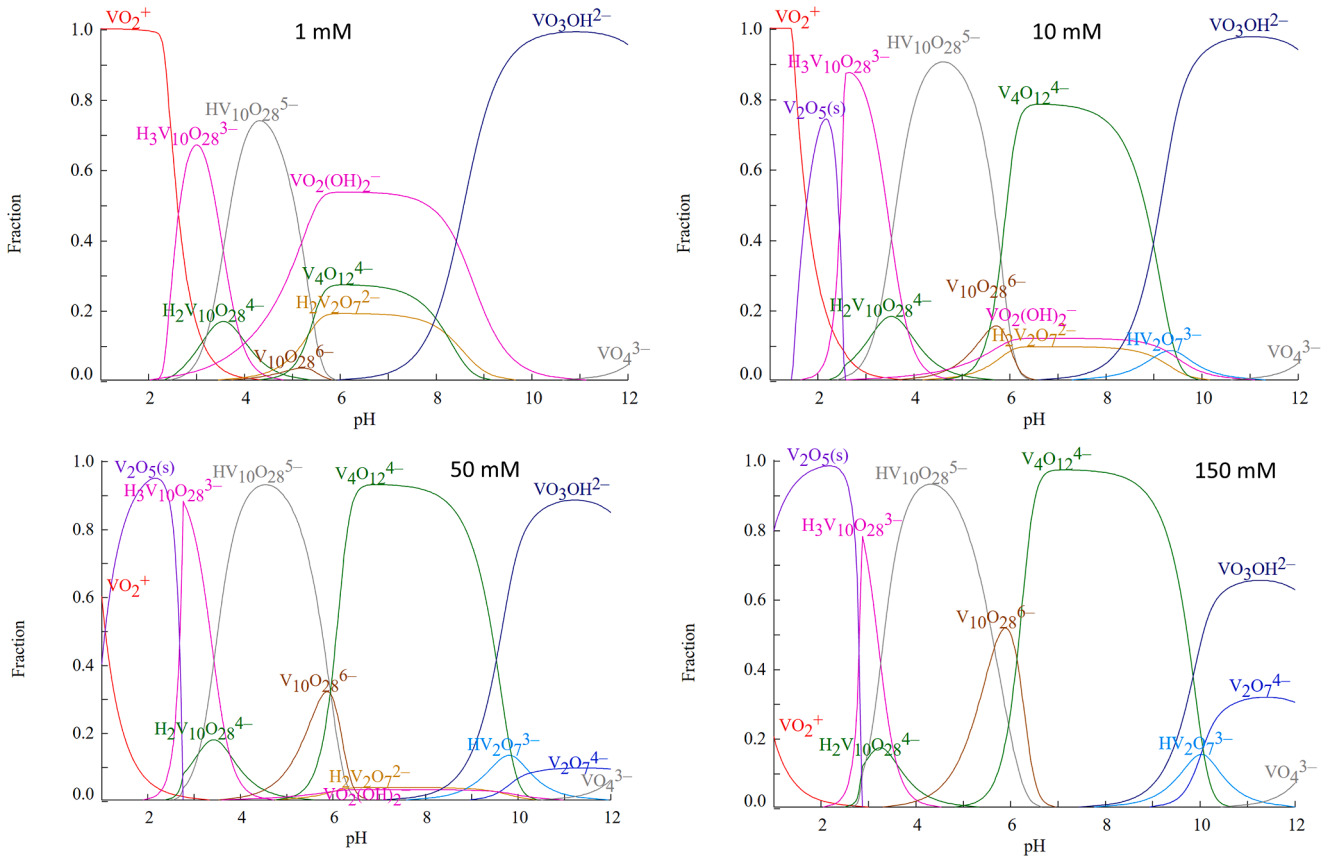

Fig. 2. Fraction vs. pH for different concentrations of $NaVO_3$ (1, 10, 50 and 150 mM) in 0.1 M NaCl solution. The diagrams were generated using Medusa software. Equilibrium log(*c*) vs. pH diagrams calculated for all concentrations investigated are given in Fig. S2.

3.3. The effect of molybdate and vanadate anions added to NaCl solutions on the composition and morphology of the sample surface

3.3.1. SEM/EDS

SEM images of the samples' surface are given in Fig. 9 for as-prepared diamond-ground sample and samples immersed for 2 h in 0.1 M NaCl, 0.1 M NaCl+ 150 mM $NaVO_3$ and 0.1 M NaCl+ 150 mM Na_2MoO_4. The composition deduced from EDS spectra taken at different spots at the surface is given in Table 2. The diamond-ground sample shows a smooth matrix surface with IMPs within the clad layer (Fig. 9a). AA1230 alloy clad layer contains over 99.3 wt.% Al (Table 1, site 1); IMPs are based mainly on Fe and Si (sites 2 and 3), with the size of between several hundred nanometres and 1 μm. Those containing Fe appear bright in Compo mode (site 2), and those containing mainly Si (site 3) appear similar to the matrix as they are much lighter than Fe. At some spots, the oxygen concentration was larger (site 3), indicating that these spots are preferentially spontaneously oxidized.

After 2 h immersion in 0.1 M NaCl, the sample surface was covered with a thicker oxide layer, exhibiting a nodular-like morphology (Fig. 9b). The layer was mainly homogenous when imaged in SE mode, but defects in the form of trenching occurred at several spots, as visible in Compo mode. Trenching is related to the corrosion process in chloride solution. EDS analysis confirmed that these spots are Fe-rich IMPs (sites 5 and 6), representing cathodic sites relative to the surrounding matrix surface (site 4). Due to the excessive formation of hydroxyl ions, the surrounding matrix surface dissolves, forming trenches [80]. The more detailed images of Fe- and Fe-Si IMPS are given in Fig. S3.

After immersion for 2 h in the solution containing vanadate ions, the surface appeared non-corroded, confirming the inhibition action of vanadate ions (Fig. 9c). The layer morphology is rather smooth, almost like the diamond-ground sample's (Fig. 9a). At IMPs, a low concentration of vanadium was detected (site 8). In contrast, at the matrix, no V could be detected using EDS, indicating that, if present, the layer of vanadium oxide was too thin to be detected using a 15 kV beam (site 7). EDS analysis was conducted at different acceleration voltages (Fig. S4) and could be detected only at IMPs at 7 kV but not at 5 kV; however, the quantification of V concentration is unreliable due to significant errors. Therefore, EDS is not an appropriate technique for characterising such a thin layer. Instead, XPS was used, as shown in the text below.

A different situation is encountered for molybdate ions (Fig. 9d). After immersion for 2 h, the surface also appeared non-corroded, without trenching, confirming that added molybdate ions act inhibitory. The layer appeared thick since no polishing mark could be observed. The layer consisted of differently-sized nodules, as observed in the SE image. The Compo image shows that the layer grown above IMPs (site 11) was rich in Mo, reaching up to 15 at.% (Table 2). A high oxygen concentration of 61 at.% (compared to ca. 7 at.% in uninhibited solution) confirms the formation of an abundant oxide layer, mainly related to molybdenum oxide. At the same time, the concentration of Al was reduced to 16 at.% indicating that the molybdenum oxide formed is overlying the Al oxide. At another IMP, Fe-Si-based (site 10), the Mo concentration was smaller, indicating that the growth of the layer is strongly dependent on the electrochemical activity of the sites at the surface and is thicker at the most active IMPs. Additional proof for substantial layer thickness is cracking around IMPs. At the matrix (site 9), the Mo concentration is smaller than at IMPs but detectable by EDS, in contrast to the layer formed in the vanadate solution (Fig. 9c).

The formation of the layer formed in the presence of molybdate was analysed further using different acceleration voltages and cross-section analysis. Fig. 10 shows the sample surface imaged and analysed by EDS at 5 kV and 15 kV (Fig. 10). When imaged at a smaller voltage of 5

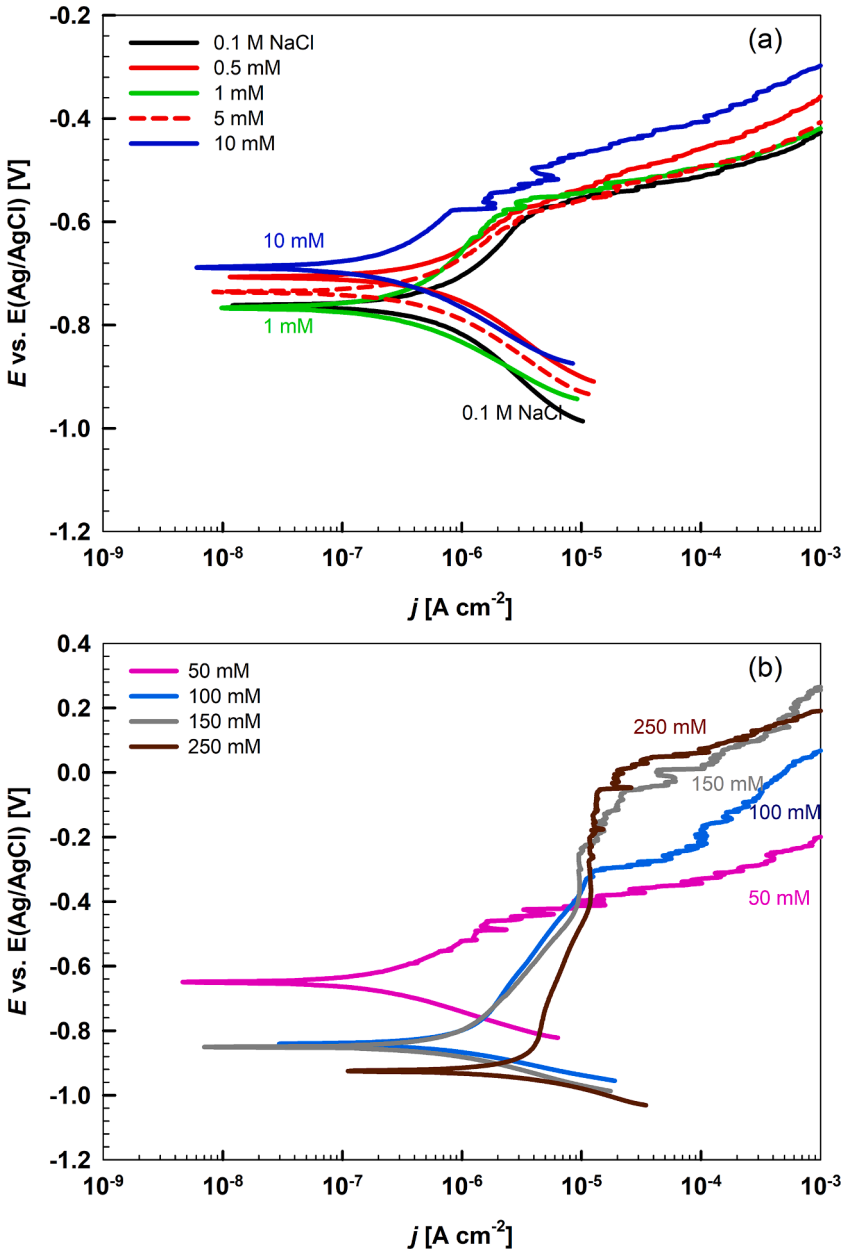

Fig. 3. Potentiodynamic polarization curves recorded for clad AA2024-T3 in 0.1 M NaCl solution and with added Na_2MoO_4 in the concentration range from 0.5 mM to 250 mM. Measurements were made in an aerated solution at room temperature after stabilization at open circuit potential for 2 h. $dE/dt = 1$ mV/s. Deduced electrochemical parameters are presented in Fig. 4 and Table S1.

kV, the analysing depth is smaller (Fig. 10a). Accordingly, detected concentrations of Mo are higher, around 20 at.% (Table 3). The layer was homogeneous throughout the matrix, but cracking appeared at sites where the layer formed above IMPs, i.e., where it is thicker (site 2). Again, this confirms the IMPs act as initiation sites of molybdate layer formation, which then spreads all over the matrix. When imaged at 15 kV (Fig. 10b), i.e. with larger analysing depth, the concentration of Mo can still be detected at all sites, i.e. at the matrix and at smaller (sites 4 and 6) and larger domes (site 5). Importantly, at the largest Mo-containing spot, Fe was detected, proving that the layer was the thickest when formed above Fe-containing IMP (site 5).

The cross-section analysis was conducted on one of the thicker spots (domes) at the surface, as presented in Fig. S5. Once the material was removed, the cross-section showed that the thick dome was formed above Fe-Si-containing IMP within the clad layer. SEM images of the cross-section are presented in Fig. 11; results of complemented EDS analysis conducted at the numbered spots are presented in Table 4. The large dome, ca. 0.7 μm thick, contained predominantly Mo-oxide and some Al (Fig. 11a, spot 1). The presence of some Al within the dome (Table 4) suggests its selective dissolution from the Fe-Si IMP; on its outward path, it is trapped with a growing Mo-oxide layer. The edge of IMP within the dome is also covered by Mo-oxide (site 4 given in detail), but is concentration is lower than within the dome and similar to that at the outside matrix (sites 5 and 6 in Fig. 11b). The dome is edged by cracks (marked by blue arrows) formed probably due to internal stress within the thick and fast-growing dome. The surrounding matrix is covered by a homogeneous Mo-oxide layer, but its thickness, ranging around 100–150 nm, is much smaller than above IMPs (Fig. 11b).

The cross-section at the middle of the dome was further described by EDS line analysis. EDS spectra recorded at site 1 (dome), site (4) (intermediate area between IMP and dome), and sites 5 and 6 (matrix) are presented in Fig. 11c. Interesting behaviour is observed in the

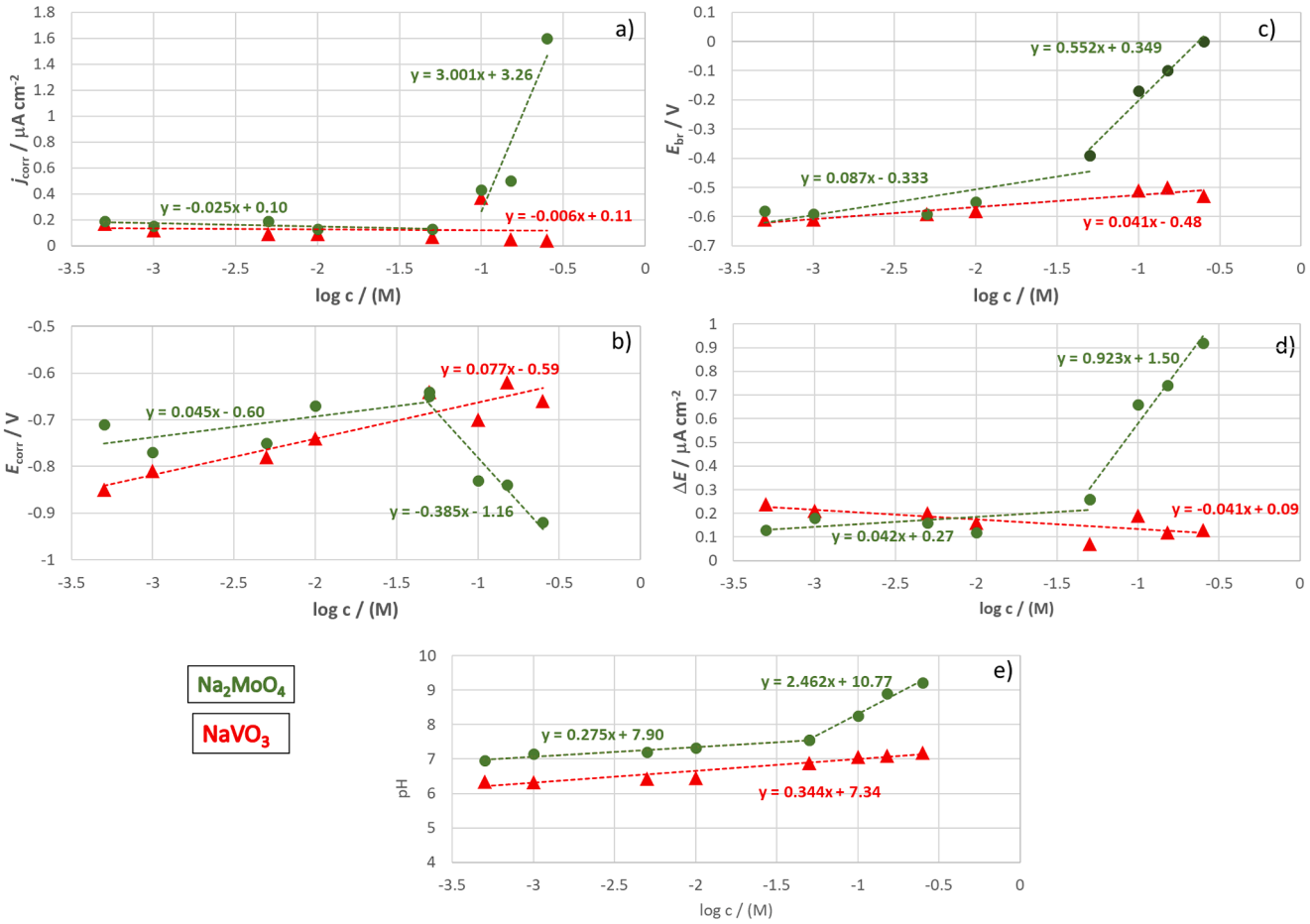

Fig. 4. (a–d) Electrochemical parameters (j_{corr}, E_{corr}, E_{br}, ΔE) deduced from potentiodynamic polarization curves (Figs. 3 and 5) and (e) pH presented as a function of the logarithm of the concentration of $NaVO_3$ and Na_2MoO_4 added to 0.1 M NaCl (concentration in M).

intermediate area (4); here Al oxide prevails over Mo-oxide indicating that the top of Fe-Si-IMP was subjected to selective dissolution of Al. Since IMPs are spots where a cathodic oxygen reduction reaction occurs, dissolved Al ions can be precipitated as Al-hydroxide in an alkaline environment. A similar mechanism, including selective dissolution of Al and Mg from Fe- and Mg-based IMPs, was noticed during the forming of cerium conversion layers on AA7075 [81]. On the contrary, with the dome (site 1), Mo-oxide is a predominant oxide.

Elemental EDS mapping across the middle of the dome and underlying IMP is presented in Fig. 12. Elemental mapping confirms that the bottom part, i.e. IMP, consists of Al, Fe and Si. Mo and O are the main elements in the dome area.

3.3.2. XPS

The composition of surface layers deduced from XPS spectra is presented in Table 5, and survey spectra are presented in Fig. S6. Spectra were recorded on diamond-ground clad AA2024-T3 and after immersion for 2 h in 0.1 M NaCl with and without added Na_2MoO_4 and $NaVO_3$. The as-prepared surface contained only Al and O; after immersion in NaCl, some Cl was also detected. When formed in NaCl with added inhibitors, the signal of Al was less intense, especially for molybdate. Since the analysis depth of XPS (<10 nm) is much smaller than for EDS (ca. 1 µm), the Al signal indicates that either layers formed in inhibitor solutions are thinner than 10 nm or that the layer formed is a mixture of Al and Mo- and V-oxides, respectively.

Devonvoluted high-resolution spectra for Al 2p, O 1s, Mo 3d and V 2p are presented in Figs. 13 and 14. Details of component peak parameters (binding energy, width, tail parameters and Gaussian/Lorentzian ratio) and fitting procedure are given in Table S5. Al 2p spectra were fitted using four peaks denoting Al metal centred at 71.5 eV, suboxide AlO_x at 73.4 eV, Al_2O_3 at 74.0 eV and $Al(OH)_3$ at 74.8 eV, respectively [82]. After grinding, surface oxide, a native oxide/hydroxide layer of AlO_x, Al_2O_3 and $Al(OH)_3$ is formed, which is thinner than 10 nm since the peak of Al metal is still present (Fig. 13). Deconvolution of O 1s peak was carried out using three peaks denoting oxide 530.1 eV, hydroxide at 531.5 eV and adsorbed water at 532.5 eV, respectively (Fig. 13). The hydroxyl contribution prevails over oxide [83].

After 2 h in NaCl, the Al metal peak disappeared, AlO_x was reduced, and the oxide contained mainly Al_2O_3 and $Al(OH)_3$. In addition, a small Cl 2p peak is identified, indicating that some chloride remained in the layer (Fig. S7). The centres of Cl $2p_{3/2}$ and $2p_{1/2}$ peaks were located at 198.4 eV and 199.7 eV, which is consistent with the formation of chloride compounds: CuCl (198.4 eV,199.1 eV), $CuCl_2$ (198.7 eV, 199.2 eV, 199.4 eV) or, presumably, oxychloride [84].

With immersion in the molybdate-containing solution, the oxide formation is even more pronounced than in the uninhibited solution. The intensity of the Al 2p peak was reduced to only 4 at.%, and oxide and hydroxide components of the O 1s spectrum increased due to the formation of Mo-oxide (Fig. 13). We did not attempt to fit the O 1s peak using component peaks of two oxides, i.e. Al- and Mo-oxide and relied on metal peaks. The deconvolution of the Mo 3d spectrum (Fig. 14) is demanding, as evidenced by a complex shape revealing that it is integrated of peaks of more than one oxidation state. Therefore, the layer formed is not univalent but consists of Mo species of different valencies. Mo(VI) species exhibit $3d_{5/2}$ and $3d_{3/2}$ peaks at 232.5 eV and 235.6 eV ascribed to MoO_3 [19,26,85]. Mo(IV) species in the form of MoO_2 exhibit $3d_{5/2}$ and $3d_{3/2}$ peaks at 229.3 eV and 232.5 eV, respectively [85,86]. In addition, the 3d peak of Mo(IV) species is reported to be

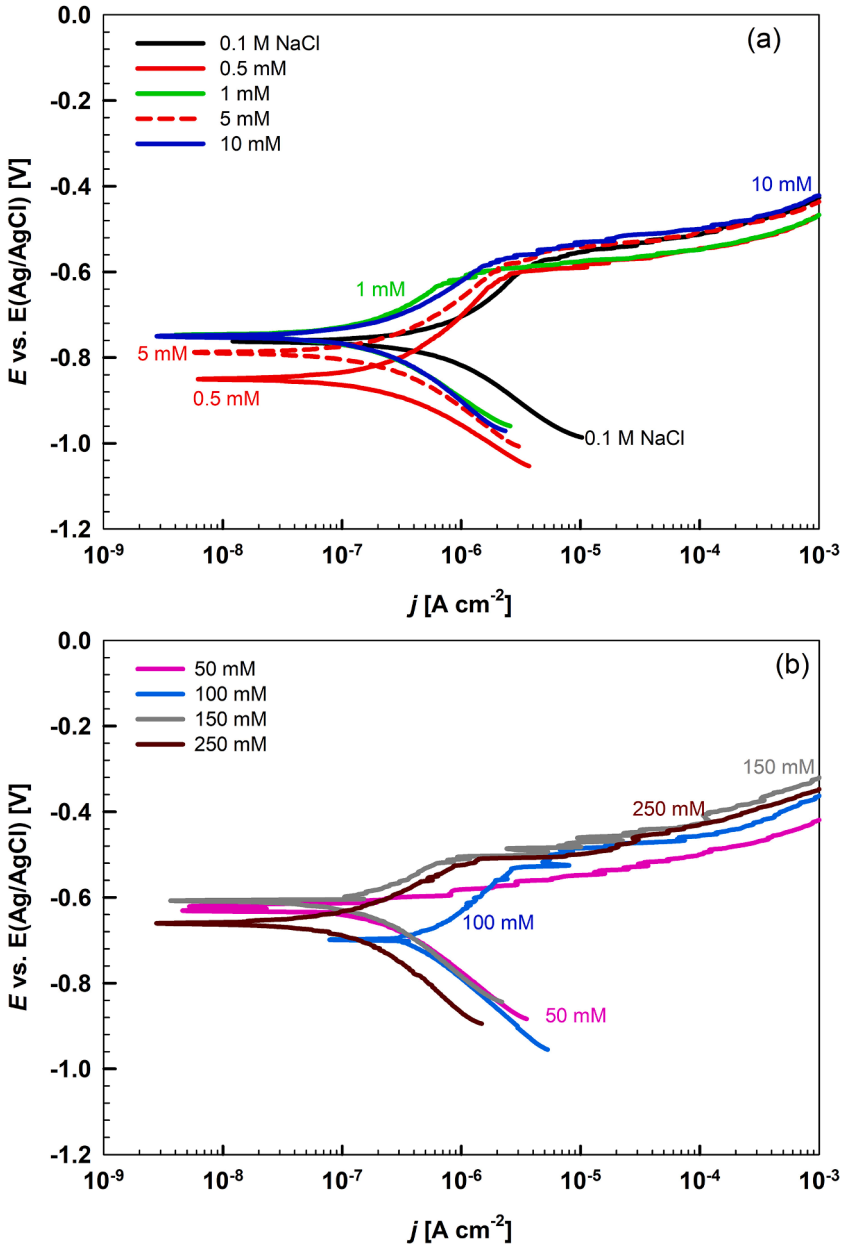

Fig. 5. Potentiodynamic polarization curves recorded for clad AA2024-T3 in 0.1 M NaCl solution and with added $NaVO_3$ in the concentration range from 0.5 mM to 250 mM. Measurements were made in an aerated solution at room temperature after stabilization at open circuit potential for 2 h. $dE/dt = 1$ mV/s. Deduced electrochemical parameters are presented in Fig. 4 and Table S2.

asymmetric, containing additional peaks ascribed to electron-pair excitations around the Fermi level induced by the appearance of the core hole, at 1.7 eV and 4.9 eV above the $3d_{5/2}$ peak [85]. These additional peaks are broader than the main $3d_{5/2}$ and $3d_{3/2}$ peaks [85]. The experimental spectrum for Mo 3d (Fig. 14) was deconvoluted using synthetic component peaks in line with literature data, i.e. two peaks related to Mo(VI) and four peaks related to Mo(IV) species. However, even when deconvoluting the experimental Mo 3d spectrum using these six component peaks, the agreement between the experimental and fitted curve was still unsatisfactory, and another pair of peaks was added, which can be justified by the literature [85]. This pair is provisionally ascribed to mixed valence oxide close to Mo_2O_5 (as proposed in ref. [85], or, possibly, with the incorporation of MoO_4^{2-} species, as proposed in ref. [19]). The final deconvoluted spectrum thus consisted of eight peaks ascribed to Mo(IV) at 229.9, 231.0, 232.2 and 234.6 eV, Mo(V) at 231.1 and 233.8 eV, and Mo(VI) at 233.0 and 235.9 eV. Based on the area of component peaks used for the deconvolution, the distribution of oxides is as follows: Mo(IV) oxide 50 %, Mo(VI) oxide 33 % and Mo(V) oxide 17 %.

Moshier and Davis used six peaks (three doublets) to describe the experimental spectra: MoO_2, MoO_4^{2-} and MoO_3 with the $3d_{5/2}$ peaks at 229.7 eV, 231.6 eV and 233.4 eV, respectively [19]. At low MoO_4^{2-} concentrations and near neutral pH, the film consisted mainly of MoO_2, whereas at higher MoO_4^{2-} concentrations, the film consisted mainly of molybdate [19]. Lopez-Garrity and Frankel deconvoluted experimental spectra using four peaks (two doublets) ascribed to MoO_2 and MoO_3 with the $3d_{5/2}$ peaks at 229.9 eV and 232.6 eV [26]. Kharitonov et al. described the experimental spectrum using six peaks (three doublets) to describe the experimental spectrum: MoO_2, Mo_2O_5 and MoO_3 with the $3d_{5/2}$ peaks at 229.2 eV, 229.9 eV and 232.7 eV, respectively [24]. Based on these considerations, it is justified to conclude that the oxide layer formed in molybdate solution contains oxides in at least two oxidation

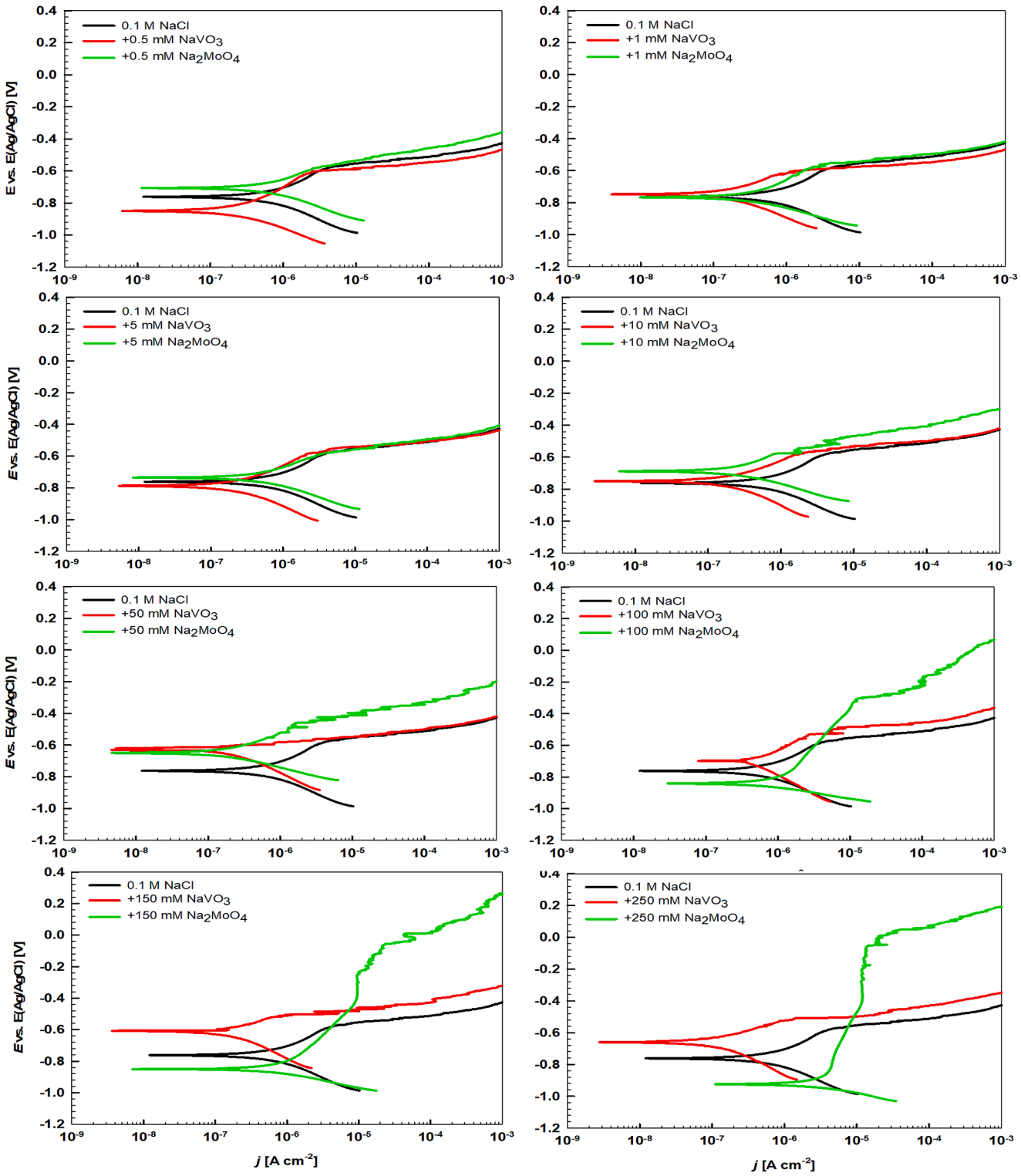

Fig. 6. Potentiodynamic polarization curves recorded for clad AA2024-T3 in 0.1 M NaCl solution and with added $NaVO_3$ and Na_2MoO_4 in the concentration range from 0.5 mM to 250 mM. Measurements were made in an aerated solution at room temperature after stabilization at open circuit potential for 2 h. $dE/dt = 1$ mV/s. Deduced electrochemical parameters are presented in Fig. 4 and Tables S1 and S2.

states, i.e. it is a mixed oxide of MoO_2 and MoO_3, possibly with the incorporation of MoO_4^{2-} species or intermediate oxide close to Mo_2O_5. The reduction of Mo(VI) species, which proceeds preferentially over Fe-Si-based IMPs which act as local cathodes [24,26], can take place according to the reaction [87]:

$$[MoO_4]^{2-} + 4H^+ + 2e^- \longrightarrow MoO_2 + 4OH^-,\ E^\circ = -0.780\ \text{V vs. SHE} \quad (8)$$

To reveal the exact nature of the oxides within the layer is beyond the scope of this study and would require additional surface analytical, possibly in situ tools, since the composition may be affected by the ex-situ nature of the sample preparation and air transfer to the spectrometer.

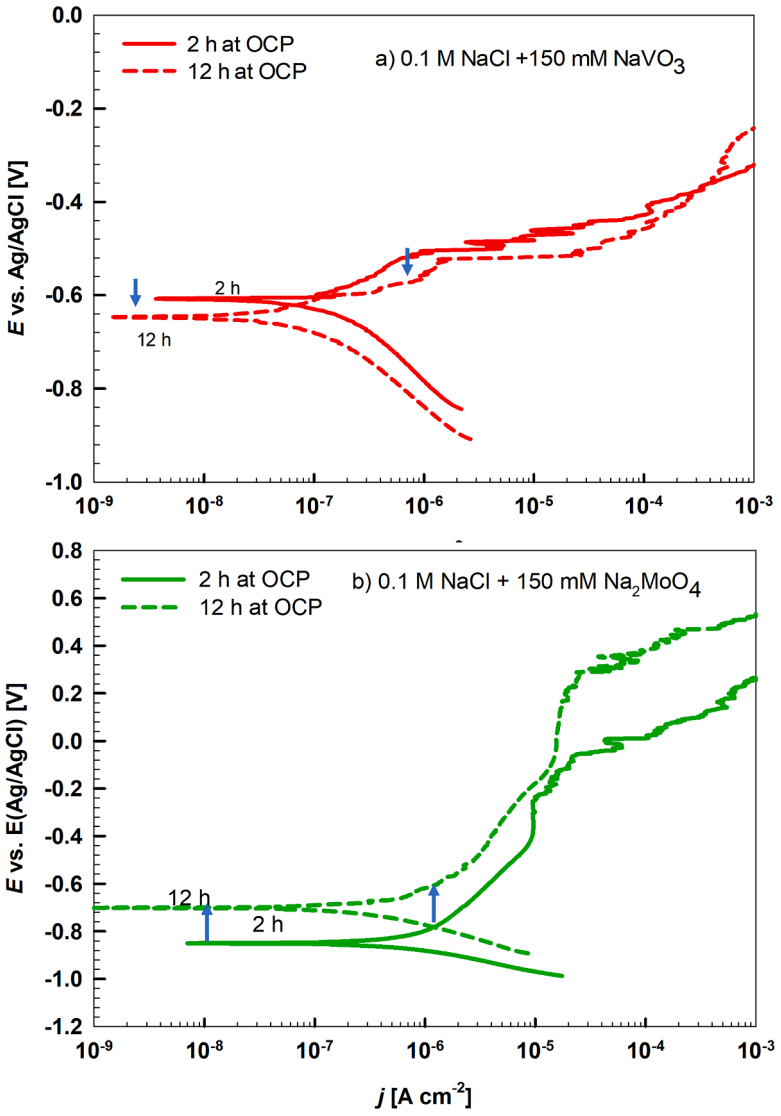

Fig. 7. Potentiodynamic polarization curves recorded for clad AA2024-T3 in 0.1 M NaCl solution with added (a) 150 mM $NaVO_3$ and (b) 150 mM Na_2MoO_4 after stabilization at open circuit potential for 2 h and 12 h. Measurements were made in an aerated solution at room temperature. Deduced electrochemical parameters are presented in Table S3.

After immersion in vanadate-containing NaCl solution, the intensity of the Al 2p peak decreased and comprised mainly $Al(OH)_3$ (Fig. 13). The increase in intensity at ca. 71 eV is related to the last part of V 3s peak (denoted by arrow). Although no vanadium was identified by EDS (Table 2), XPS analysis identified vanadium at the surface, confirming that the layer formed was too thin to be detected by EDS (at least when using 15 kV). Therefore, XPS confirmed the formation of V oxide (Fig. 14). Experimental V 2p spectrum was deconvoluted using two $2p_{3/2}$–$2p_{1/2}$ doublets, i.e. for V_2O_5 at 517.1 eV and 524.2 eV, and VO_2 at 516.1 eV and 524.2 eV, in agreement with the literature [88,89]. These doubles achieved satisfactory agreement with experimental data, and we did not introduce additional possible doublets related to V_2O_3 with $2p_{3/2}$ at 515.1 eV and V_6O_{13} at 516.9 eV [88], also due to the relatively narrow E_b range to achieve reliable data. XPS thus corroborated that V oxide is formed in at least two oxidation states, V(V) and V(IV). Based on the area of component peaks used for the deconvolution, the distribution of oxides is as follows: V(IV) oxide 43 %, V(V) oxide 57 %.

The present findings are in line with results by Kharitonov et al. [56], who proposed a two-step mechanism of corrosion inhibition on AA6063-T5 in which V(V) species are first reduced to V(IV) or V(III) above cathodic IMPs and then oxidized to mixed-valence V(V)/V(IV) polymerized compounds. V(III) species were detected by confocal Raman spectroscopy, while XPS detected V(V) and V(IV) [56], as in the present study. The following reaction was proposed for the reduction of adsorbed vanadium(V) species [56]:

$$[V_nO_{3n}]^{n-} + 2nH^+ + ne^- \longrightarrow nVO_2 + nH_2O \ (n = 3, 4, 5) \quad (9)$$

The shape of O 1s in vanadate-containing solution differed from that in uninhibited solution (Fig. 13); the peak centre shifted to lower E_b, and the component oxide peak increased, indicating the formation of additional oxide. Since the concentration of Al was reduced to almost one-half compared to the uninhibited NaCl solution, we can assume that at least half of the oxide/hydroxide component is related to the formation of vanadium oxide. As for molybdate, we did not attempt to fit the O 1s peak using component peaks of two oxides, i.e. Al- and V-oxide, since their positions are very closed and relied on the V 2p peak.

3.4. Corrosion inhibition mechanism of clad AA2024-T3 by molybdate and vanadate anions

Differences in the behaviour of molybdate and vanadate as corrosion inhibitors are related to both their aqueous chemistry and their

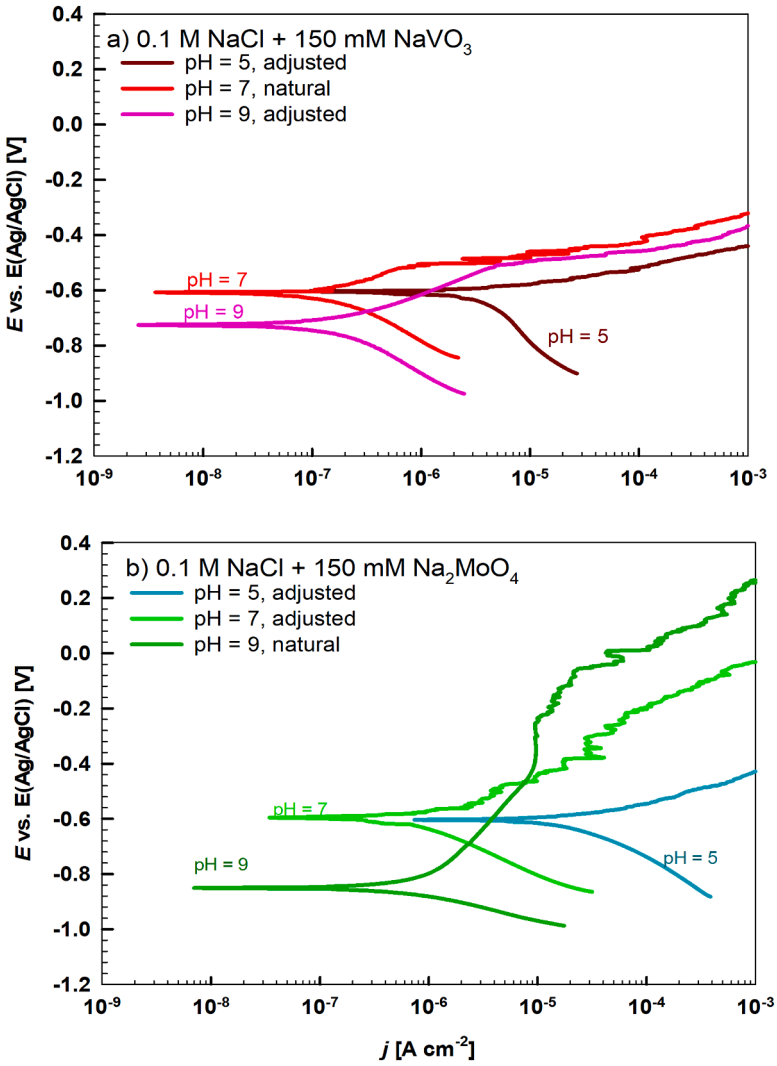

Fig. 8. Potentiodynamic polarization curves recorded for clad AA2024-T3 in 0.1 M NaCl solution with added (a) 150 mM $NaVO_3$ (pH = 7) and (b) 150 mM Na_2MoO_4 (pH = 9). Measurements were conducted also in solutions with adjusted pH (5 and 9 for vanadate and 5 and 7 for molybdate). Measurements were made in an aerated solution at room temperature after stabilization at open circuit potential for 2 h. Deduced electrochemical parameters are presented in Table S4.

behaviour as adsorbed species at the clad alloy surface. Milošev described the differences in the corrosion mechanisms of molybdate inhibition on Al metal and Al alloys [13]. Fig. 15a illustrates the possible mechanism of molybdate inhibition (150 mM) on clad alloy containing Fe-Si IMPs postulated based on the experimental evidence gained in this study. The mechanism is similar to Al alloys, where the Al-oxide-covered matrix acts as an anode, and Fe-Si IMPs are cathodic sites. On the oxide-covered-Al matrix surface, the adsorption of Cl^- and subsequent formation of $AlCl_4^-$ complexes generates defects or flaws in the Al oxide layer, acting as the preferential adsorption sites for molybdate adsorption [21]. On the matrix, adsorption of molybdate does not necessarily lead to its reduction but causes the blocking of flaws and, thereby, corrosion inhibition. The adsorbed molybdate layer is thick, as evidenced by SEM. This is reflected in the Mo XPS 3d signal comprising ca. half of Mo(VI) component (Fig. 14). In contrast, on Fe-Si IMPs, which represent cathodic sites, adsorbed molybdate is partially reduced to Mo (IV) oxide, thus rapidly leading to the mitigating of the cathodic activity and thus inhibition of corrosion. The reduction proceeds to MoO_2 and/or $MoO{\cdot}(OH)_2$ (Fig. 15b).

$$3MoO_4^{2-} + 6H^+ + 2Al \rightarrow 3MoO_2 + Al_2O_3{\cdot}3H_2O \quad (10)$$

$$3MoO_4^{2-} + 12H^+ + 6e^- \longrightarrow 3MoO{\cdot}(OH)_2 + 3H_2O \quad (11)$$

Reduced molybdate in (IV) form is not the final product. Based on XPS data, it is evident that Mo oxide formed comprised not only Mo(IV) but also (V) (and (VI). One plausible explanation is that the reduction to Mo(IV) is followed by subsequent oxidation to Mo(V)/(VI), allowing the formation of molybdenum oxide with several oxidation states.

The reduction of molybdate, however, leads to local acidification [26]. Under acidic conditions, condensation and polymerisation of molybdate species ($Mo_7O_{24}^{6-}$, $Mo_8O_{26}^{4-}$) occur, as described in [13], and subsequent oxidation to intermediate oxides such as Mo_4O_{11} [26], reactions (1, 13, 14). It can be hypothesised that these polymerised oxides are formed in trenches around the IMPs due to local acidification.

$$3MoO_4^{2-} + 6H^+ + 2Al \longrightarrow 3MoO_2 + Al_2O_3{\cdot}3H_2O \quad (12)$$

$$8MoO_2 + 6H_2O \longrightarrow 2Mo_4O_{11} + 12H^+ + 12e^- \quad (13)$$

$$5MoO_4^{2-} + 14H^+ + 14e^- \longrightarrow MoO{\cdot}(OH)_2 + Mo_4O_{11} + 6H_2O \quad (14)$$

The formation of a thick Mo oxide with varying oxidation and polymerisation states, especially at concentrations above 50 mM, is responsible for the effective inhibitive action on clad 2024-T3 alloy. This is related to the significantly increased content of molybdate as a prevailing species at pH 9 (Fig. 1). The oxide covers the whole sample

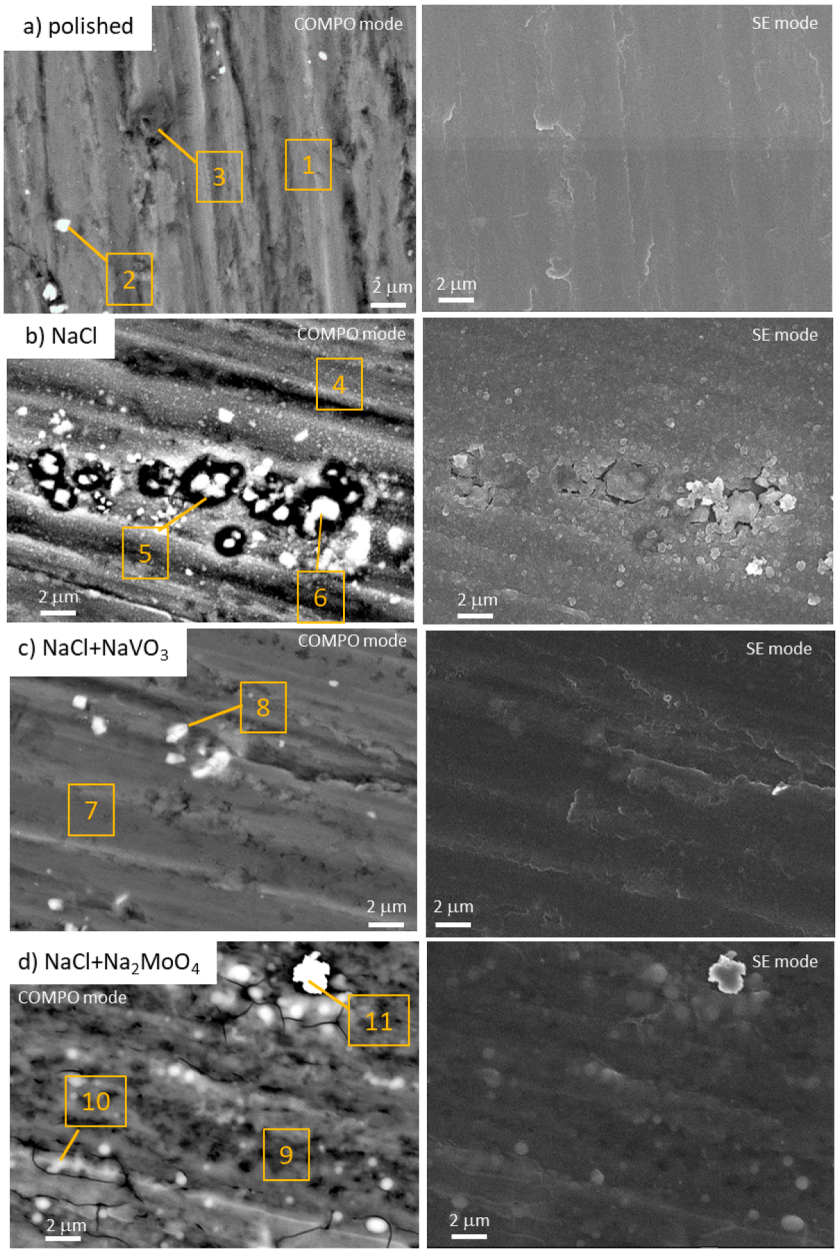

Fig. 9. SEM images recorded in Compo and SE modes are given on the left and right panels, respectively. Images were recorded on (a) diamond-ground clad AA2024-T3 samples and after immersion for (b) 2 h in 0.1 M NaCl, (c) d) 2 h in 0.1 M NaCl+ 150 mM $NaVO_3$ and (d) 2 h in 0.1 M NaCl+ 150 mM Na_2MoO_4. The acceleration voltage was 15 kV. Numbers mark the spots where EDS analysis was carried out; the results are given in Table 2.

surface, matrix and IMPs and represents a strong barrier for the ingress of chloride ions, reflected in a broad passive range.

In contrast to molybdate, the oxide layer formed in the presence of vanadate in NaCl solution is much thinner in the comparative concentration range. Despite that, it mitigates the dissolution in the region around E_{corr}, as evidenced by an almost one-decade smaller j_{corr} than in the presence of molybdate (Fig. 6). However, this layer cannot withstand larger overpotentials, and the layer is susceptible to localized breakdown at the same or slightly more positive potential as the uninhibited solution. Unlike in molybdate-containing solution, the increased concentration does not lead to broadening the passive region. Namely, in the investigated concentration range between 0.5 mM and 250 mM, the pH of the NaCl solution with added vanadate is between 6 and 7 and does not change significantly with concentration (Fig. 2) but affects the $j_{corr,}$ which is linearly reduced. Both molybdate and vanadate are primarily anodic inhibitors.

Fig. 15b illustrates the possible mechanism of vanadate inhibition on clad alloy containing Fe-Si IMPs. Under comparative conditions of concentration and immersion time, there is a striking difference between molybdate and vanadate in the thickness of the layer formed. For the former, a thick layer is formed throughout the surface covering the matrix and IMP, whereas for vanadate, a very thin layer was formed on the matrix (not identifiable by EDS) and somewhat thicker at the IMPs. Similar to molybdate, vanadate may adsorb at the flaws and blocks the reactive sites at the matrix. Immersion time at E_{oc} produces a lesser effect on vanadate than on molybdate solution. This leads to the conclusion that the kinetics of vanadate adsorption is vital for blocking the defects in the oxide layer. The adsorption is more extensive at IMPs, where a thin layer of V oxide is detected. The metavanadates are the prevailing species at a pH value of around 7. XPS corroborated that V oxide is formed in at least two oxidation states, V(V) [VO_4^{3-}, $V_3O_9^{3-}$, $V_4O_{12}^{4-}$, $VO_2(OH)_2^-$, VO_3OH^{2-}] and V(IV) [$V_4O_9^{2-}$ and $V_5O_{15}^{5-}$]. However,

Table 2
Chemical composition (in atomic %) deduced by EDS analysis at enumerated sites, tagged on the SEM images in Fig. 9.

Site	Concentration (at.%)						
	Al	O	Si	Fe	V	Mo	Na
Diamond-ground sample							
1	93.2	6.8	–	–	–	–	–
2	87.8	4.2	–	8.0	–	–	–
3	54.3	30.4	15.3	–	–	–	–
Immersed for 2 h in 0.1 M NaCl							
4	92.5	7.5	–	–	–	–	–
5	63.4	18.3	3.6	14.7	–	–	–
6	80.5	6.0	0.5	13.0	–	–	–
Immersed for 2 h in 0.1 M NaCl+ 150 mM $NaVO_3$							
7	95.2	4.8	–	–	–	–	–
8	77.3	12.5	2.1	7.8	(0.3)	–	–
Immersed for 2 h in 0.1 M NaCl+ 150 mM Na_2MoO4							
9	85.0	13.7	–	–	–	1.3	–
10	52.9	36.0	2.1	2.6	–	5.4	1.0
11	16.3	61.5	–	2.9	–	15.5	3.8

at concentrations above 50 mM, the presence of decavanadates is predicted by the equilibrium diagrams (Fig. 2), which are known to be ineffective inhibitors [26].

Metavanadates were proven effective inhibitors exhibiting strong inhibition of ORR at a level similar to chromate [50]. The reduction of metavanadate solution was very slow, so it was proposed that the inhibition is a consequence of the adsorption of the metavanadate and not

Table 3
Chemical composition (in atomic %) deduced by EDS analysis at enumerated sites, tagged on the SEM images in Fig. 10. EDS analysis was conducted at 5 kV (spots 1, 2) and 15 kV (spots 3–6).

Site	Concentration (at.%)				
	Al	O	Fe	Mo	Na
Immersed for 2 h in 0.1 M NaCl+ 150 mM Na_2MoO_4					
1	31.4	50.3	–	15.9	2.4
2	19.1	56.0	–	21.4	3.5
3	82.9	14.8	–	2.0	0.3
4	73.6	21.4	–	4.4	0.6
5	68.8	24.8	0.6	5.2	0.6
6	79.4	17.5	–	2.7	0.4

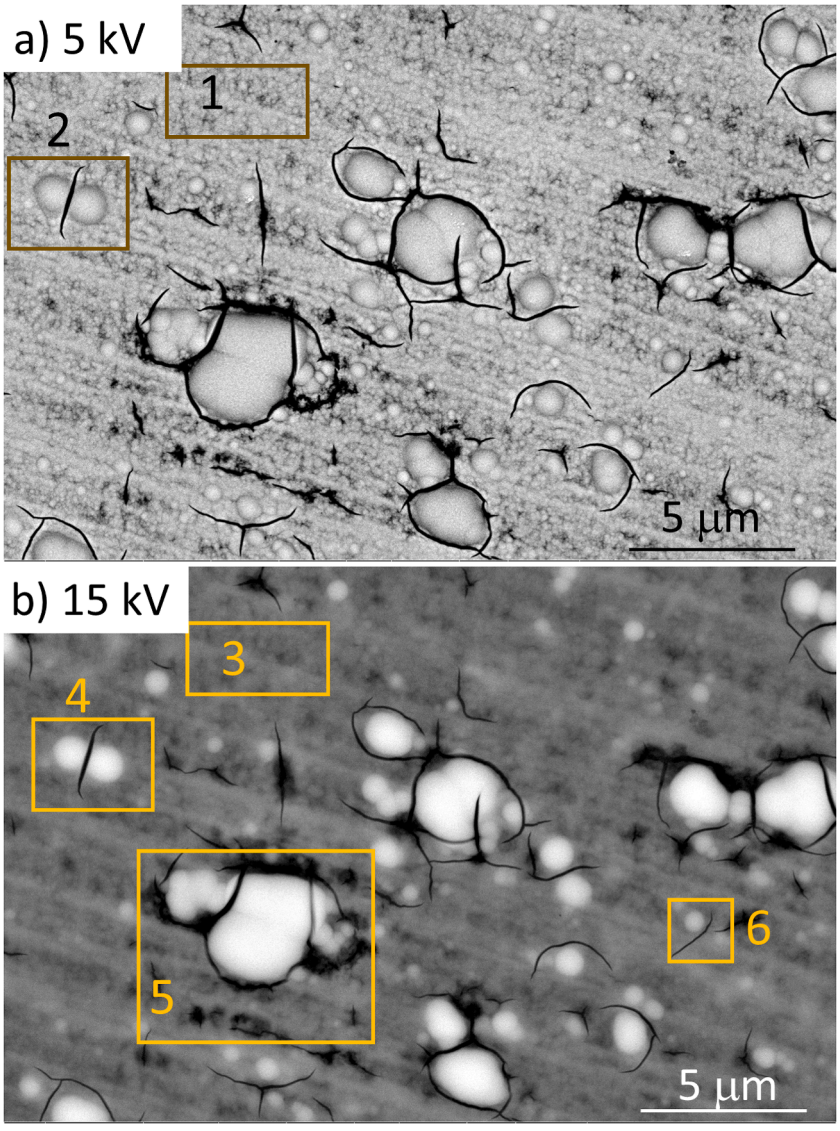

Fig. 10. SEM images recorded in Compo mode on diamond-ground clad AA2024-T3 samples after immersion for 2 h in 0.1 M NaCl+ 150 mM Na_2MoO_4. The acceleration voltage was (a) 5 kV and (b) 15 kV. Numbers mark the spots where EDS analysis was carried out; the results are given in Table 3.

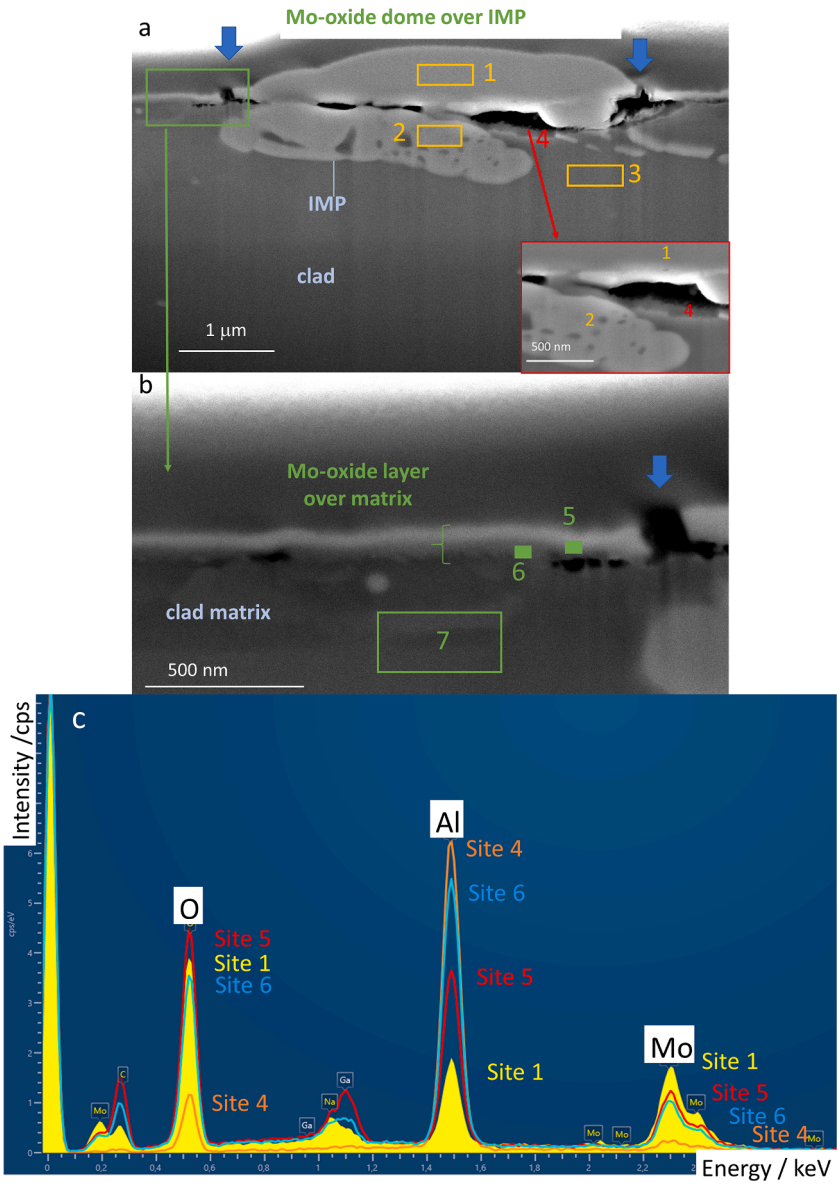

Fig. 11. SEM images of the cross-section made across one of the larger domes of Mo-oxide, as shown in Fig. S5. (a) Mo-oxide dome (site 1) is formed above Fe-Si IMP (site 2) within clad (site 3). Mo-oxide is also present at site 4, enlarged in red-marked detail. (b) The enlarged area of the site green-marked in (a) shows the Mo-oxide layer (sites 5, 6) formed over the clad matrix where no IMP is present (site 7). Blue arrows mark the crack at the edge of the dome. SEM and EDS analyses were conducted at 5 kV. Results of EDS analysis at marked numbered spots are presented in Table 4. (c) EDS spectra showing O, Al and Mo signals at sites 1, 4, 5 and 6.

Table 4
Chemical composition (in atomic %) deduced by EDS analysis at enumerated sites, tagged on the SEM images in Fig. 11. The sum is not 100 % because Ga and C were not considered in the table.

Site	Concentration (at.%)					
	Al	O	Fe	Si	Mo	Na
	Immersed for 2 h in 0.1 M NaCl+ 150 mM Na_2MoO_4					
1	17.8	41.4	–	–	31.5	2.3
2	69.4	6.7	16.4	3.8	–	–
3	92.4	4.4	–	–	–	–
4	80.6	13.2	–	–	5.0	–
5	27.7	32.7	–	–	17.0	2.6
6	43.8	26.4	–	–	15.0	2.0
7	92.4	4.2	–	–	–	–

from the formation of reduced species. Metavanadate was shown to adsorb on the surface following a Langmuir isotherm with a critical concentration of 0.05 mM [52]. Kharitonov et al. reported that after 24 h immersion in NaCl containing 3 mM $NaVO_3$, a micrometre-thick layer was formed consisting of V(IV) and V(V) polymerized species, especially on IMPs on AA6063-T5 [56]. It was suggested that V(V) is first reduced to V(IV) or V(III) and then oxidized to a mixed-valence (V)/(IV) polymerized compound with an amorphous bottom layer and a crystalline outer layer [56]. The precipitate film was thinner on the oxide-covered Al matrix [56], similar to this study. In the present work, the film was much thinner (2 h immersion), which was not indicative that prolonged immersion time to 12 h significantly affected the effect.

A contributing factor to the better effectiveness of molybdate over vanadate may be the higher pH of NaCl solution upon adding molybdate, reaching almost 9. Namely, it was reported that the Al passive oxide layer is stable between 4 and 10 with an almost constant thickness of ca. 4 nm [90]. In the passive range, however, the chloride concentration within the layer decreased linearly as a function of pH, reaching a minimum at

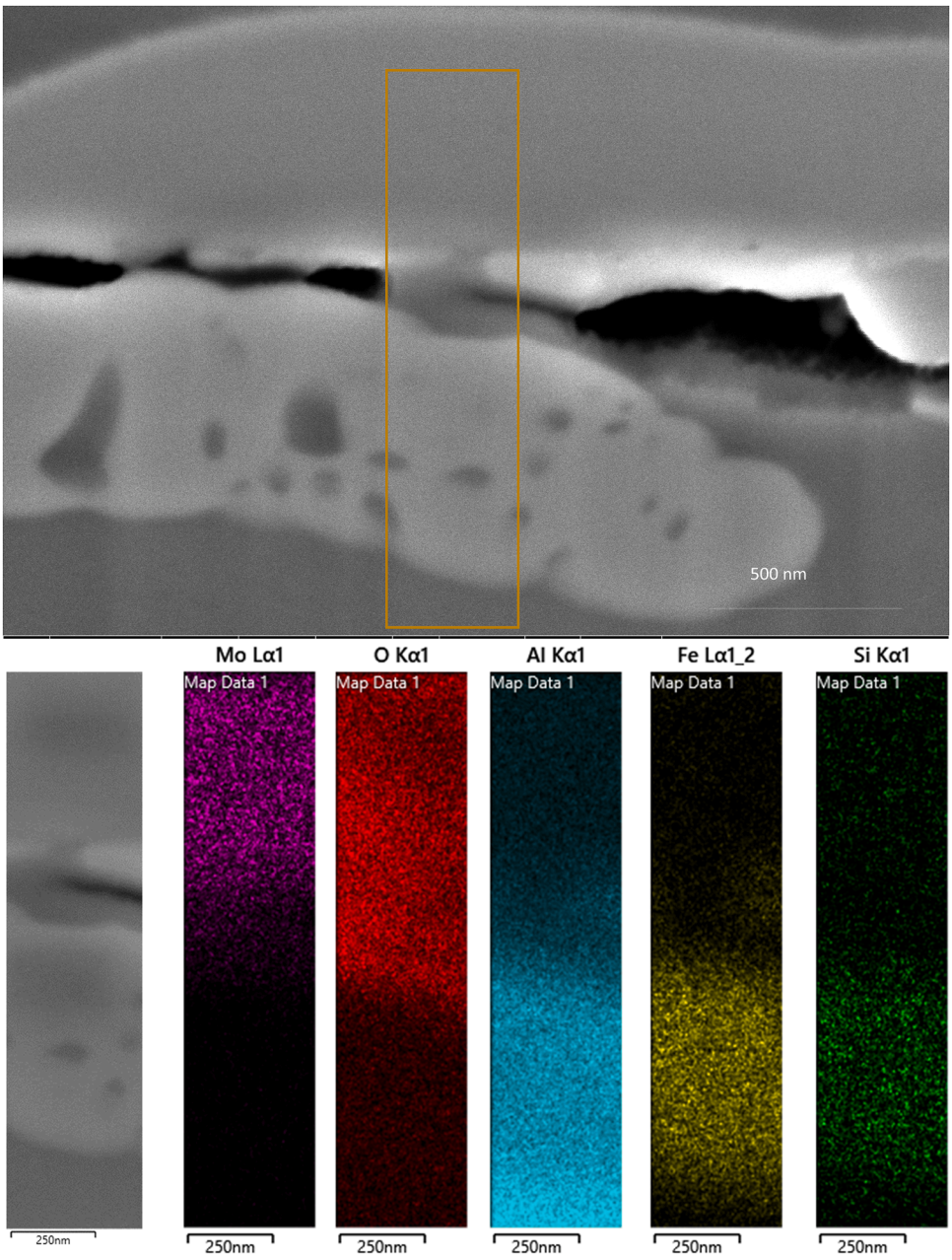

Fig. 12. SEM image of the cross-section with the area where EDS elemental mapping is made in the brown-marked rectangle. Elemental maps for Mo, O, Al, Fe and Si are given in the lower raw.

Table 5
Chemical composition (in atomic %) deduced by XPS analysis (Figs. 13 and 14).

	Concentration (at.%)				
	Al (2p)	O (1s)	Cl (2p)	V (2p)	Mo (3d)
diamond-ground	20.1	79.9	–	–	–
2 h NaCl	20.0	77.8	2.2	–	–
2 h in 0.1 M NaCl+ 150 mM $NaVO_3$	13.3	72.3	–	13.1	–
2 h in 0.1 M NaCl+ 150 mM $NaVO_3$	4.5	74.9	–	–	17.7

around 10 [90]. Chloride deposition includes chloride accumulation on the surface and in the passive film. This may imply that the number of defects/ flaws may be smaller in the solution containing molybdate with a pH of around 9 than that containing vanadate with a pH of around 7.

Finally, it should be noted that the identification of the exact nature of the polymerised species is beyond the scope of this study and should involve additional structure-sensitive techniques.

4. Conclusions

Aluminium alloy 2024-T3 clad with aluminium oxide (AA1023) is susceptible to corrosion in chloride solutions, mainly due to intermetallic Fe-Si particles acting as cathodic sites on the surrounding Al oxide matrix. Although molybdate and vanadate ions have been extensively studied on other aluminium alloys, no study on clad AA2024-T3 has been reported, especially a comparative study. Both ions are characterised by a complex chemistry in aqueous solution involving mononuclear and polynuclear ions and are highly dependent on pH and concentration. In the concentration range tested (0.5–250 mM), vanadium is present in solution mainly as metavanadate, but also as

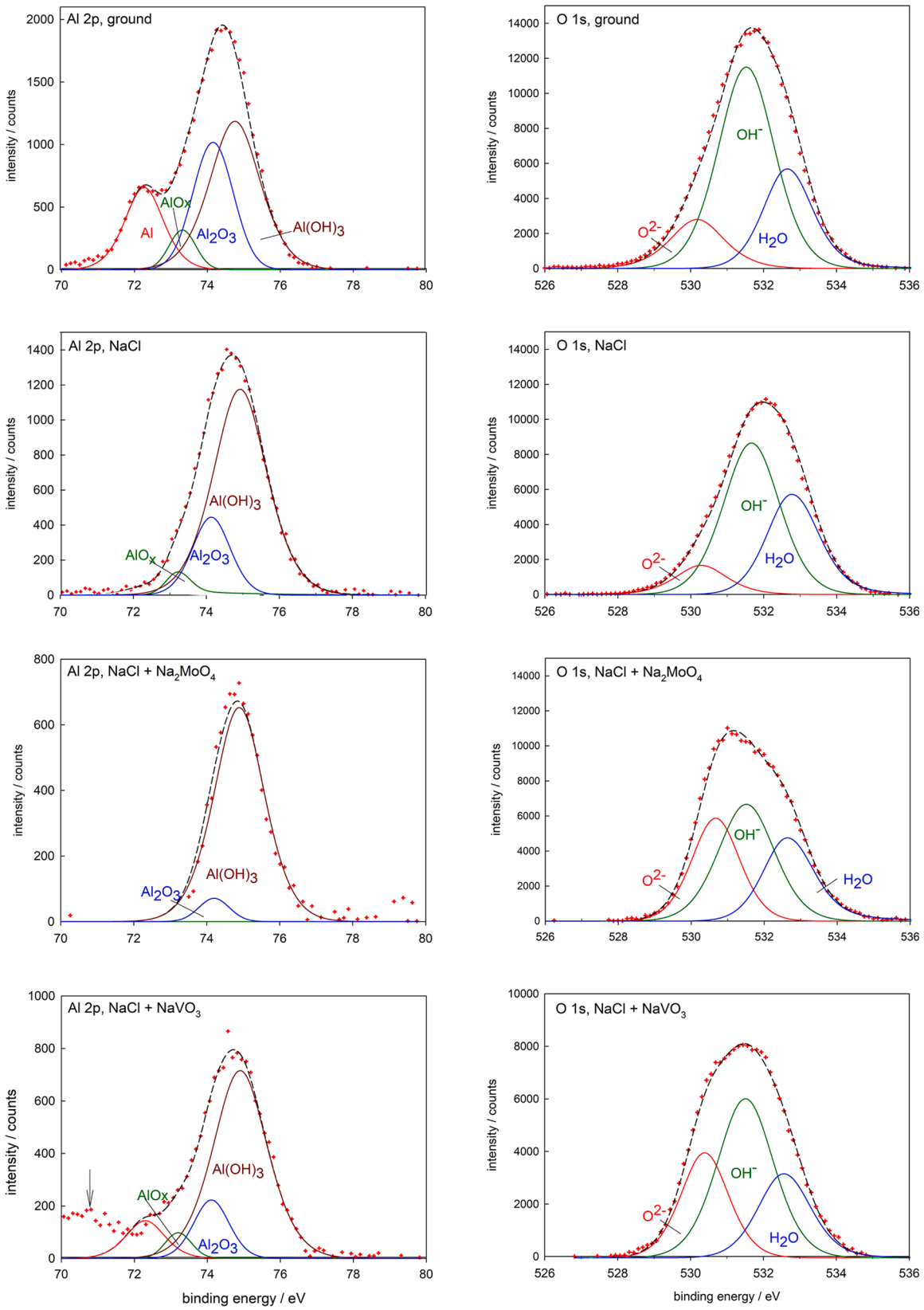

Fig. 13. XPS high-resolution spectra (Al 2p and O 1s) recorded on diamond-ground clad AA2024-T3 samples and after 2 h immersion in 0.1 M NaCl, 0.1 M NaCl+ 150 mM $NaVO_3$, and 0.1 M NaCl+ 150 mM Na_2MoO_4. Red cross—experimental data, dashed curve—fitted curve, solid lines—component peaks used for fitting.

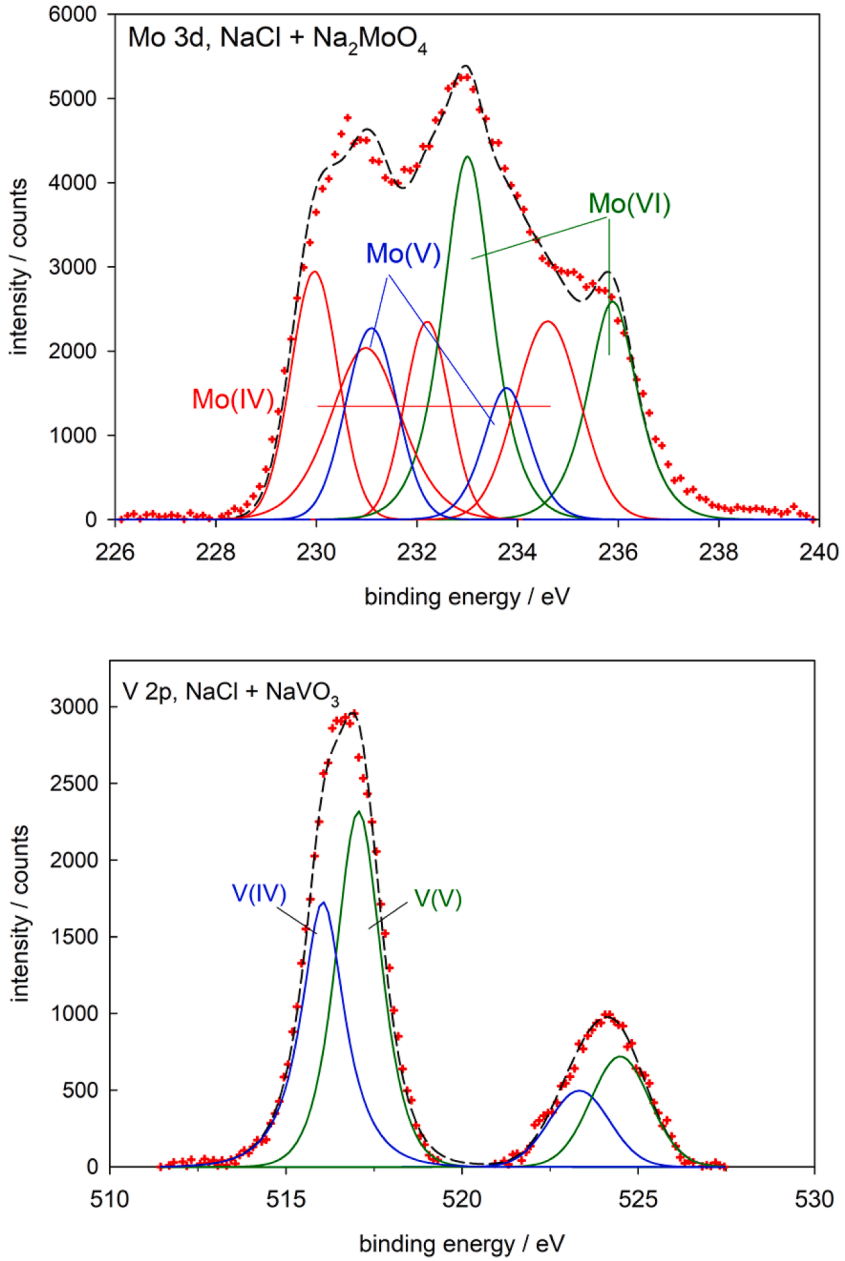

Fig. 14. XPS high-resolution spectra (Mo 3d and V 2p) recorded on diamond ground clad AA2024-T3 samples after 2 h immersion in 0.1 M NaCl+ 150 mM Na_2MoO_4 and NaCl+ 150 mM $NaVO_3$. Red cross—experimental data, dashed curve—fitted curve, solid lines—component peaks used for fitting.

decavanadate at higher concentrations. While the former are efficient inhibitors, the latter are not. The adsorption of metavanadates leads to corrosion inhibition, but the greater proportion of decavanadates at higher concentrations slows down the effect. In contrast, the effectiveness of molybdate as a corrosion inhibitor increases steeply above 50 mM, as the species MoO_4^{2-} and $HMoO_4^-$ predominate at pH above 7.5. Once adsorbed, they are involved in subsequent reduction reactions to form Mo(IV) and possibly in reoxidation to form Mo(V)/(VI).

The potentiodynamic polarization curves for the $c_{inhibitor} \leq 50$ mM are quite similar and show a slight decrease in j_{corr} and no significant shift in E_{br} compared to the uninhibited 0.1 M NaCl solution. However, with a $c_{inhibitor} > 50$ mM, molybdate leads to a strong expansion of the passive region to 1.6 V, accompanied by an increase in j_{corr}. Increasing the concentration does not change the trend for vanadate, which induces a smaller j_{corr} but a much narrower passive range than molybdate. The effect of molybdate benefits from the prolonged immersion in the open circuit potential for 12 h; a small shift in the negative direction was observed for vanadate. Both ions primarily inhibit the anodic reaction.

The pH value of the solution has a strong influence on the inhibitory effect of the two ions. After addition of the highest vanadate concentration, the pH value changes to 7.2. In contrast,the addition of molybdates at $c > 50$ mM shifts the pH value to 9.2 and thus contributes to the stability of the natural Al oxide formed. The inhibitory effect of molybdate at a natural pH of 9 decreases when the pH drops to 7. The reverse is true for vanadate. Both ions become activators when the pH of the solution drops to 5 due to the prevalence of polynuclear Mo species and decavanadates, respectively.

SEM/EDS analysis confirms that the layers formed in 0.1 M NaCl with 150 mM vanadate and molybdate differ greatly in thickness, with the latter being much thicker. The formation of the V-oxide layer is restricted to the Fe-Si-based IMPs, while the formation of the Mo-oxide layer is distributed throughout the IMPs and the matrix, being thickest on the former, as shown by the cross-section SEM. XPS analysis enabled the speciation of the oxide layers formed and thus contributed to a better

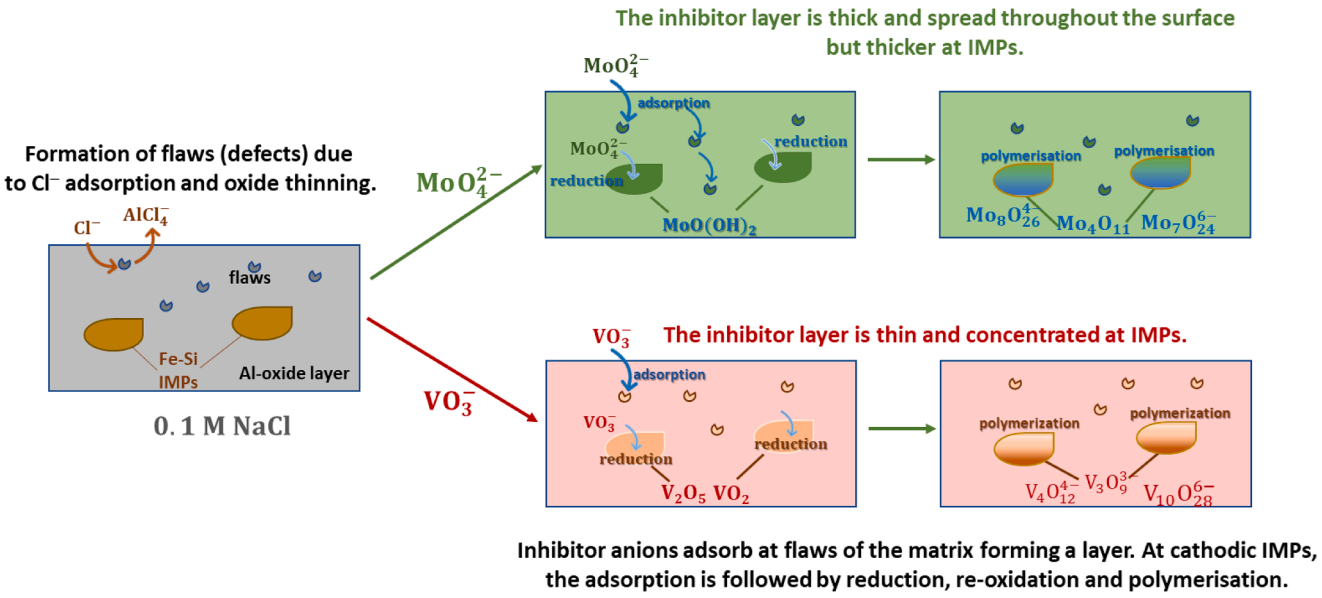

Fig. 15. Proposed mechanism of inhibition of corrosion of clad AA2024 in chloride solution by molybdate and vanadate (150 mM).

understanding of the inhibition mechanism. The reduction of molybdate and subsequent oxidation to higher valence leads to the formation of the oxide layer with mixed valences. Similarly, V oxide with mixed valences of (IV) and (V) is formed. Identifying the exact nature of the polymerised species is beyond the scope of this study and should involve additional structure-sensitive techniques.

CRediT authorship contribution statement

Ingrid Milošev: Writing – review & editing, Supervision, Methodology, Funding acquisition, Formal analysis, Data curation, Conceptualization. **Tjaša Pavlovčič:** Methodology, Formal analysis, Data curation. **Matija Tomšič:** Writing – review & editing, Supervision, Methodology, Funding acquisition, Formal analysis.

Declaration of competing interest

The authors declare that they have no known competing financial interests or personal relationships that could have appeared to influence the work reported in this paper.

Data availability

Data will be made available on request.

Acknowledgements

The authors acknowledge the financial support from the Slovenian Research and Innovation Agency (research core funding nos. P2-0393 and P1-0201, and project no. N1-0308 “Nanoplastics in aqueous environments: structure, migration, transportand remediation”). The authors thank Prof. J. Kovač and T. Filipič, MSc, of the Department of Surface Engineering, for conducting XPS analyses. Barbara Kapun, BSc, and Ana Kraš, MSc of the Department of Physical and Organic Chemistry, are acknowledged for conducting SEM/EDS analyses and additional construction of concentration vs. pH diagrams, respectively. Access to scientific equipment (SEM/EDS/FIB) of the Centre of Excellence in Nanoscience and Nanotechnology—Nanocenter, Ljubljana, is acknowledged.

Supplementary materials

Supplementary material associated with this article can be found, in the online version, at doi:10.1016/j.electacta.2024.144893.

References

[1] M. Kendig, R.G. Buchheit, Corrosion inhibition of aluminum and aluminum alloys by soluble chromates, chromate coatings, and chromate-free coatings, Corrosion 59 (2003) 379–400, https://doi.org/10.5006/1.3277570.
[2] B.R.W. Hinton, Metal Finish. 89/9 (1991) 55–61.
[3] B.R.W. Hinton, Metal Finish. 89/10 (1991) 15–20.
[4] O. Gharbi, S. Thomas, C. Smith, N. Birbilis, Chromate replacement: what does the future hold? npj Mater. Degrad. 2 (2018) 12, https://doi.org/10.1038/s41529-018-0034-5.
[5] S. Zhao, N. Birbilis, Searching for chromate replacements using natural language processing and machine learning algorithms, npj Mater. Degrad. 7 (2023) 2, https://doi.org/10.1038/s41529-022-00319-0.
[6] L. Wang, G.-H. Zhang, J. Dang, K.-C. Chou, Oxidation roasting of molybdenite concentrate, Trans. Nonferrous Met. Soc. China 25 (2015) 4167–4174, https://doi.org/10.1016/S1003-6326(15)64067-5.
[7] IARC monographs on the evaluation of carcinogenic risks to humans, in: Welding, Molybdenum trioxide, and Indium Tin Oxide, 118, International Agency for Research on Cancer, Lyon, France, 2018.
[8] IARC monographs on the evaluation of carcinogenic risks to humans, in: Cobalt in Hard Metals and Cobalt Sulfate, Gallium Arsenide, Indium Phosphide and Vanadium Pentoxide, 86, World Health Organization and International Agency for Research on Cancer, Lyon, France, 2006.
[9] IARC monographs on the evaluation of carcinogenic risks to humans. a) vol. 49: Chromium, Nickel and Welding, Lyon, France (1990).
b) vol. 100C: Arsenic, Metals, Fibres and Dust, Lyon, France (2012). https://www.ncbi.nlm.nih.gov/books/NBK304375/.
[10] ThermoFisher Safety Data Sheet Sodium-molybdate-dihydrate.
[11] ThermoFisher Safety data Sheet Sodium vanadate.
[12] ThermoFisher Safety Data Sheet Sodium Chromate.
[13] I. Milošev, Corrosion inhibition of aluminium alloys by molybdate ions: a critical review of the chemistry, mechanisms and applications, Corros. Sci. 229 (2024) 111854, https://doi.org/10.1016/j.corsci.2024.111854.
[14] A.L. Bayes, Noncorrosive antifreeze liquid, U.S. Patent 2,147,395 (1939), https://patents.google.com/patent/US2147395.
[15] M.S. Vukasovich, J.P.G. Farr, Molybdate in corrosion inhibition—A review, Polyhedron 5 (1–2) (1986) 551–559, https://doi.org/10.1016/S0277-5387(00)84963-3.
[16] W.D. Robertson, Molybdate and tungstate as corrosion inhibitors and the mechanism of inhibition, J. Electrochem. Soc. 98 (3) (1951) 94–100. https://iopscience.iop.org/article/10.1149/1.2778118.
[17] A.M. Shams El Din, L. Wang, Mechanism of corrosion inhibition by sodium molybdate, Desalination 107 (1996) 29–43, https://doi.org/10.1016/0011-9164(96)00148-8.
[18] J. Augustynski, Passivity of metals, in: R.P. Frankenthal, J. Kruger (Eds.), Electrochemical Society, Pennington, New Jersey, 1978, p. 989.
[19] W.C. Moshier, G.D. Davis, Interaction of molybdate anions with the passive film on aluminum, Corrosion 46 (1990) 43–50, https://doi.org/10.5006/1.3585065.

[20] R.R. Wiggle, V. Hospadaruk, E.A. Styloglou, Mater. Perform. 6 (1981) 13–17.
[21] C.B. Breslin, G. Treacy, W.M. Carroll, Studies on the passivation of aluminium in chromate and molybdate solutions, Corros. Sci. 36 (1994) 1143–1154, https://doi.org/10.1016/0010-938X(94)90139-2.
[22] M.A. Jakab, F.J. Presuel-Moreno, J.R. Scully, Effect of molybdate, cerium, and cobalt ions on the oxygen reduction reaction on AA2024-T3 and selected intermetallics, J. Electrochm. Soc. 153 (2006) B244–D252, https://doi.org/10.1149/1.2200300.
[23] A.Kh. Bairamow, S. Zakipor, C. Leygraph, An xps investigation of dichromate and molybdate inhibitors on aluminium, Corros. Sci. 25 (1985) 69–73, https://doi.org/10.1016/0010-938X(85)90089-7.
[24] D.S. Kharitonov, I. Dobryden, B. Sefer, J. Ryl, A. Wrzesińska, I.V. Makarova, I. Bobowska, I.I. Kurilo, P.M. Claesson, Surface and corrosion properties of AA6063-T5 aluminum alloy in molybdate-containing sodium chloride solutions, Corros. Sci. 171 (2020) 108658, https://doi.org/10.1016/j.corsci.2020.108658.
[25] S. Zein El Abedin, Role of chromate, molybdate and tungstate anions on the inhibition of aluminium in chloride solutions, J. Appl. Electrochem. 31 (6) (2001) 711–718, https://doi.org/10.1023/A:1017587911095.
[26] O. Lopez-Garrity, G.S. Frankel, Corrosion inhibition of aluminum alloy 2024-T3 by sodium molybdate, J. Electrochem. Soc. 161 (3) (2014) C95–C106, https://doi.org/10.1149/2.044403jes.
[27] B.D. Chambers, S.R. Taylor, M.W. Kendig, Rapid discovery of corrosion inhibitors and synergistic combinations using high-throughput screening methods, Corrosion 61 (5) (2005) 480–489, https://doi.org/10.5006/1.3280648.
[28] B.D. Chambers, S.R. Taylor, High-throughput assessment of inhibitor synergies on aluminium alloy 2024-T3 through measurement of surface copper enrichment, Corrosion 63 (3) (2007) 268–276, https://doi.org/10.5006/1.3278353.
[29] B.D. Chambers, S.R. Taylor, The high throughput assessment of aluminium alloy corrosion using fluorometric methods. Part II—A combinatorial study of corrosion inhibitors and synergistic combinations, Corros. Sci. 49 (3) (2007) 1597–1609, https://doi.org/10.1016/j.corsci.2006.08.006.
[30] S.R. Taylor, B.D. Chambers, Identification and characterization of nonchromate corrosion inhibitor synergies using high-throughput methods, Corrosion 64 (3) (2008) 255–270, https://doi.org/10.5006/1.3278470.
[31] M. Khobaib, L. Quakenbush, C.T. Lynch, Effect of surfactants upon corrosion inhibition of high-strength steels and aluminum alloy, Corrosion 39 (1983) 253–257, https://doi.org/10.5006/1.3581909.
[32] O. Lopez-Garrity, G.S. Frankel, Synergistic corrosion inhibition of AA2024-T3 by sodium silicate and sodium molybdate, J. Electrochem. Soc. Lett. 3 (2014) C33–C35. https://iopscience.iop.org/article/10.1149/2.0021410eel.
[33] S.A.S. Dias, S.V. Lamaka, T.C. Diamantino, M.G.S. Ferreira, Synergistic protection against corrosion of AA2024-T3 by sol–gel coating modified with La and Mo-enriched zeolites, J. Electrochem. Soc. 161 (2014) C215–C222. https://iopscience.iop.org/article/10.1149/2.064404jes.
[34] K.A. Yasakau, J. Tedim, M. Zheludkevich, R. Drumm, M. Sheh, M. Wittmar, M. Veith, M.G.S. Ferreira, Cerium molybdate nanowires for active corrosion protection of aluminium alloys, Corros. Sci. 58 (2012) 41–51, https://doi.org/10.1016/j.corsci.2012.01.012.
[35] I.A. Kartsonakis, A.C. Balaskas, G.C. Kordas, Influence of cerium molybdate containers on the corrosion performance of epoxy coated aluminium alloys 2024-T3, Corros. Sci. 53 (2011) 3771–3779, https://doi.org/10.1016/j.corsci.2011.07.026.
[36] M. Garćia-Rubio, P. Ocón, A. Climent-Ford, R.W. Smith, M. Curioni, G. E. Thompson, P. Skeldon, A. Lavía, I. Garćia, Influence of molybdate species on the tartaric acid/sulphuric acid anodic films grown on AA2024 T3 aerospace alloy, Corros. Sci. 51 (2009) 2034–2042, https://doi.org/10.1016/j.corsci.2009.05.034.
[37] R. Subasri, K.R.C. Soma Raju, D.S. Reddy, A. Jyothirmayi, V.S. Ijeri, O. Prakash, S. P. Gaydos, Environmentally friendly Zn–Al layered double hydroxide (LDH)-based sol–gel corrosion protection coatings on AA 2024-T3, J. Coat. Res. Technol. 16 (2019) 1447–1463, https://doi.org/10.1007/s11998-019-00229-y.
[38] X.F. Liu, S.J. Huang, H.C. Gu, Corrosion protection of an aluminum alloy with nontoxic compound inhibitors in chloride media, Corrosion 58 (2002) 826–834, https://doi.org/10.5006/1.3287664.
[39] A.S. Hamdy, A.M. Beccaria, P. Traverso, Corrosion protection of AA6061 T6-10 % Al2O3 composite by molybdate conversion coatings, J. Appl. Electrochem. 35 (2005) 467–472, https://doi.org/10.1007/s10800-004-8329-3.
[40] D. Rodriguez, R. Mishra, D. Chidambaram, Molybdate-based conversion coatings for aluminum alloys part I: coating formation, ECS Trans. 45 (2013) 1–12. https://iopscience.iop.org/article/10.1149/04528.0001ecst/meta.
[41] Y. Huang, S. Mu, Q. Guan, J. Du, Corrosion resistance and formation analysis of a molybdate conversion coating prepared by alkaline treatment on aluminum alloy 6063, J. Electrochem. Soc. 166 (2019) C224–C230. https://iopscience.iop.org/article/10.1149/2.1111908jes.
[42] C.-S. Liang, Z.-F. Lv, Y.-L. Zhu, S.-A. Xu, H. Wang, Protection of aluminium foil AA8021 by molybdate-based conversion coatings, Appl. Surf. Sci. 288 (2014) 497–502, https://doi.org/10.1016/j.apsusc.2013.10.060.
[43] D. Walker, G.D. Wilcox, Molybdate based conversion coatings for zinc and zinc alloy surfaces: a review, Trans. Inst. Metal Finish. 86 (2008) 251–259, https://doi.org/10.1179/174591908X345022.
[44] G.D. Wilcox, D.R. Gabe, M.E. Warwick, The role of molybdates in corrosion prevention, Corros. Rev. 6 (1986) 327–365.
[45] W. Guixiang, Z. Milin, W. Ruizhi, Molybdate and molybdate/permanganate conversion coatings on Mg–8.5Li alloy, Appl. Surf. Sci. 258 (2012) 2648–2654, https://doi.org/10.1016/j.apsusc.2011.10.112.
[46] H. Guan, R.G. Buchheit, Corrosion protection of aluminum alloy 2024-T3 by vanadate conversion coatings, Corrosion 60 (2004) 284–296, https://doi.org/10.5006/1.3287733.
[47] K.D. Ralsoton, S. Chrisanti, T.L. Young, R.G. Buchheit, Corrosion inhibition of aluminum alloy 2024-T3 by aqueous vanadium species, J. Electrochem. Soc. 155 (2008) C350–C359. https://iopscience.iop.org/article/10.1149/1.2907772/pdf.
[48] K.D. Ralsoton, R.G. Buchheit, An initial exploration of corrosion inhibition of AA6061 and AA7075 by aqueous vanadate, J. Electrochem. Soc. Lett. 2 (9) (2013) C35–C38. https://iopscience.iop.org/article/10.1149/2.005309eel.
[49] J. Li, B. Hurley, R. Buchheit, Inhibition performance study of vanadate on AA2024-T3 at high temperature by SEM, FIB, Raman and XPS, J. Electrochem. Soc. 162 (2015) C219–C227. https://iopscience.iop.org/article/10.1149/2.0371506jes/meta.
[50] M. Ianuzzi, T. Young, G.S. Frankel, Aluminum alloy corrosion inhibition by vanadates, J. Electrochem. Soc. 153 (2006) B533–B541. https://iopscience.iop.org/article/10.1149/1.2358843.
[51] M. Ianuzzi, G.S. Frankel, Inhibition of aluminum alloy 2024 corrosion by vanadates: an in situ atomic force microscopy scratching investigation, Corrosion 63 (2007) 672–688, https://doi.org/10.5006/1.3278417.
[52] M. Ianuzzi, G.S. Frankel, Mechanisms of corrosion inhibition of AA2024-T3 by vanadates, Corros. Sci. 49 (2007) 2371–2391, https://doi.org/10.1016/j.corsci.2006.10.027.
[53] S.C. Morton, G.S. Frankel, Atmospheric pitting corrosion of AA7075-T6 under evaporating droplets with and without inhibitors, Mater. Corr. 65 (2014) 351–361, https://doi.org/10.1002/maco.201307363.
[54] D.S. Kharitonov, I.I. Kurilo, A. Wrzesińska, I.M. Zharskii, Corrosion inhibition of AA6063 alloy by vanadates in alkaline media, Mat.-Wiss. Werkstofftech. 48 (2017) 646–660, https://doi.org/10.1002/mawe.201600752.
[55] D.S. Kharitonov, C. Örnek, P.M. Claesson, J. Sommertune, I.M. Zharskii, I.I. Kurilo, J. Pan, Corrosion inhibition of aluminum alloy AA6063-T5 by vanadates: microstructure characterization and corrosion analysis, J. Electrochem. Soc. 165 (2018) C116–C1126. https://iopscience.iop.org/article/10.1149/2.0341803jes.
[56] D.S. Kharitonov, J. Sommertune, C. Örnek, J. Ryl, I.I. Kurilo, P.M. Claesson, J. Pan, Corrosion inhibition of aluminium alloy AA6063-T5 by vanadates: local surface chemical events elucidated by confocal Raman micro-spectroscopy, Corros. Sci. 148 (2019) 237–250, https://doi.org/10.1016/j.corsci.2018.12.011.
[57] J. Tedim, S.K. Poznyak, A. Kuznetsova, D. Raps, T. Hack, M.L. Zheludkevich, M.G. S. Ferreira, Enhancement of active corrosion protection via combination of inhibitor-loaded nanocontainers, ACS Appl. Mater. Interfaces 2 (2010) 1528–1535, https://doi.org/10.1021/am100174t.
[58] M.L. Zheludkevich, S.K. Poznyak, L.M. Rodrigues, D. Raps, T. Hack, L.F. Dick, T. Nunes, M.G.S. Ferreira, Active protection coatings with layered double hydroxide nanocontainers of corrosion inhibitor, Corros. Sci. 52 (2010) 602–611, https://doi.org/10.1016/j.corsci.2009.10.020.
[59] Y. Zhang, P. Yu, J. Wu, F. Chen, Y. Li, Y. Zhang, Y. Zuo, Y. Qi, Enhancement of anticorrosion protection via inhibitor-loaded ZnAlCe-LDH nanocontainers embedded in sol–gel coatings, J. Coat. Technol. Res. 15 (2018) 303–313, https://doi.org/10.1007/s11998-017-9978-6.
[60] K.A. Yasakau, A. Kuznetsova, S. Kallip, M. Starykevich, J. Tedim, M.G.S. Ferreira, M.L. Zheludkevich, A novel bilayer system comprising LDH conversion layer and sol–gel coating for active corrosion protection of AA2024, Corros. Sci. 143 (2018) 299–313, https://doi.org/10.1016/j.corsci.2018.08.039.
[61] M. Yu, X. Zhao, L. Xiong, B. Xue, X. Kong, J. Liu, S. Li, Improvement of corrosion protection of coating system via inhibitor response order, Coatings 8 (2018) 365, https://doi.org/10.3390/coatings8100365.
[62] B. Xue, M. Yu, J. Liu, S. Li, L. Xiong, X. Kong, Synthesis of inhibitor nanocontainers with two-dimensional structure and their anticorrosion action in sol–gel coating on AA2024-T3 aluminum alloy, J. Electrochem. Soc. 164 (2017) C641–C652. https://iopscience.iop.org/article/10.1149/2.0851712jes.
[63] M.B. Jensen, M.J. Petersen, N. Jadhav, V.J. Gelling, SECM investigation of corrosion inhibition by tungstate- and vanadate-doped polypyrrole/aluminum flake composite coatings on AA2024-T3, Prog. Org. Coat. 77 (2014) 2116–2122, https://doi.org/10.1016/j.porgcoat.2014.05.019.
[64] A.S. Hamdy, I. Doench, H. Möhwald, Intelligent self-healing corrosion resistant vanadia coating for AA2024, Thin. Solid Films 520 (2011) 1668–1678, https://doi.org/10.1016/j.tsf.2011.05.080.
[65] P. Wang, X. Dong, D.W. Schaefer, Structure and water-barrier properties of vanadate-based corrosion inhibitor films, Corros. Sci. 52 (2010) 943–949, https://doi.org/10.1016/j.corsci.2009.11.017.
[66] S. Liu, G.E. Thompson, P. Skeldon, Vanadate post-treatments of anodised aluminium and AA 2024 T3 alloy for corrosion protection, Trans. Inst. Metal Finish. 96 (2018) 137–144, https://doi.org/10.1080/00202967.2018.1419629.
[67] Z. Zou, L. Ning, D. Li, Corrosion protection properties of vanadium films formed on zinc surfaces, Rare Metals 30 (2011) 146–149, https://doi.org/10.1007/s12598-011-0214-8.
[68] Z. Feng, B. Hurley, J. Li, R. Buchheit, Corrosion inhibition study of aqueous vanadate on Mg alloy AZ31, J. Electrochem. Soc. 165 (2018) C94–C102. https://iopscience.iop.org/article/10.1149/2.1171802jes/meta.
[69] T. Shulha, M. Serdechnova, S.V. Lamaka, X. Lu, C. Feiler, C. Blawert, M. L. Zheludkevich, Corrosion inhibitors intercalated into layered double hydroxides prepared in situ on AZ91 magnesium alloys: structure and protection ability, ACS Appl. Mater. Interfaces 15 (2023) 6098–6112, https://doi.org/10.1021/acsami.2c18675.
[70] Z. Gao, D. Zhang, X. Qiu, S. Jiang, Y. Wu, Q. Zhang, X. Li, The mechanisms of corrosion inhibition of hot-dip galvanized steel by vanadyl oxalate: a galvanic

corrosion investigation supported by XPS, Corros. Sci. 142 (2018) 153–160, https://doi.org/10.1016/j.corsci.2018.07.024.
[71] https://www.kth.se/che/medusa/.
[72] XFIT programme, Wolff M. Thesis, Heinrich-Heine Universität, Düsseldorf, Germany, 1992.
[73] M. Pourbaix, Atlas of Electrochemical Equilibria in Aqueous Solution, second ed., NACE, Cebelcor, Houston, TX, Brussels, 1974.
[74] J.-P. Jovilet, Metal Oxide Nanostructures Chemistry. Synthesis from Aqueous Solutions, second ed., Oxford University Press, New York, USA, 2015.
[75] P. Gouzerh, M. Che, From Scheele and Berzelius to Müller. Polyoxometalates (POMs) revisited and the ``missing link'' between the bottom up and top down approaches, L'Actualité Chimique 298 (2006) 9–22. https://new.societechimiquedefrance.fr/wp-content/uploads/2019/12/2006-298-juin-Che-p.9.pdf.
[76] P.L. Smedley, D.G. Kinniburgh, Molybdenum in natural waters: a review of occurrence, distributions and controls, Appl. Geochem. 84 (2017) 387–432, https://doi.org/10.1016/j.apgeochem.2017.05.008.
[77] J.-H. Huang, F. Huang, L. Evans, S. Glasauer, Vanadium: global (bio)geochemistry, Chem. Geol. 417 (2015) 68–89, https://doi.org/10.1016/j.chemgeo.2015.09.019.
[78] P. Rodič, I. Milošev, Corrosion inhibition of pure aluminium and alloys AA2024-T3 and AA7075-T6 by cerium(III) and cerium(IV) salts, J. Electrochem. Soc. 163 (2016) C85–C93. https://iopscience.iop.org/article/10.1149/2.0431603jes/meta.
[79] W. Zhang, G.S. Frankel, Transitions between pitting and intergranular corrosion in AA2024, Electrochim. Acta 48 (2003) 1193–1210, https://doi.org/10.1016/S0013-4686(02)00828-9.
[80] O. Schneider, G.O. Ilevbare, J.R. Scully, R.G. Kelly, In situ confocal laser scanning microscopy of AA 2024-T3 corrosion metrology II. Trench formation around particles, J. Electrochem. Soc. 151 (2004) B465–B472, https://doi.org/10.1149/1.1764781.
[81] I. Milošev, B. Kapun, P. Rodič, The relation between the microstructure of aluminum alloy 7075-T6 and the type of cerium salt in the formation of the cerium conversion layer, J. Electrochem. Soc. 169 (2022) 091501. https://iopscience.iop.org/article/10.1149/1945-7111/ac8d35/meta.
[82] I. Spajić, E. Rahimi, M. Lekka, R. Offoiach, L. Fedrizzi, I. Milošev, Al_2O_3 and HfO_2 atomic layers deposited in single and multilayer configurations on titanium and on stainless steel for biomedical applications, J. Electrochem. Soc. 168 (2021) 071510. https://iopscience.iop.org/article/10.1149/1945-7111/ac131b/meta.
[83] I. Milošev, H.-H. Strehblow, The behavior of stainless steels in physiological solution containing complexing agent studied by X-ray photoelectron spectroscopy, J. Biomed. Mater. Res. 52 (2000) 404–412, https://doi.org/10.1002/1097-4636(200011)52:2<404::AID-JBM22>3.0.CO;2-Z.
[84] I. Milošev, N. Kovačević, J. Kovač, A. Kokalj, The roles of mercapto, benzene and methyl groups in the corrosion inhibition of imidazoles on copper: I. Experimental characterization, Corros. Sci. 98 (2015) 107–118, https://doi.org/10.1016/j.corsci.2015.05.006.
[85] D.O. Scanlon, G.W. Watson, D.J. Payne, G.R. Atkinson, R.G. Egdell, D.S.L. Law, Theoretical and experimental study of the electronic structures of MoO_3 and MoO_2, J. Phys. Chem. C 114 (2010) 4636–4645, https://doi.org/10.1021/jp9093172.
[86] J. Baltrusaitis, B. Mendoza-Sanchez, V. Fernandez, R. Veenstra, N. Dukstiene, A. Roberts, N. Fairley, Generalized molybdenum oxide surface chemical state XPS determination via informed amorphous sample model, Appl. Surf. Sci. 326 (2014) 151–161, https://doi.org/10.1016/j.apsusc.2014.11.077.
[87] N. Stolica, Molybdenum, Ch. 16, in: A.J. Bard, R. Parsons, J. Jordan (Eds.), Standard Potentials in Aqueous Solution, IUPAC, Marcel Dekker, Inc, New York, Basel, 1985, p. 462.
[88] J. Mendialdua, R. Casanova, Y. Barbaux, XPS studies of V_2O_5, V_6O_{13}, VO_2 and V_2O_3, J. Electron Spectrosc. 71 (1995) 249–261, https://doi.org/10.1016/0368-2048(94)02291-7.
[89] G. Silversmit, D. Depla, H. Poelma, G.B. Marin, R. De Gryse, Determination of the V2p XPS binding energies for different vanadium oxidation states (V^{5+} to V^{0+}), J. Electron Spectrosc. 135 (2004) 167–175, https://doi.org/10.1016/j.elspec.2004.03.004.
[90] A. Kolics, A.S. Besing, P. Baradlai, R. Haasch, A. Wieckowski, Effect of pH on thickness and ion content of the oxide film on aluminum in NaCl media, J. Electrochem. Soc. 148 (7) (2001) B251–B259. https://iopscience.iop.org/article/10.1149/1.1376118.